

**McFACTS IV: Electromagnetic Counterparts to AGN Disk Embedded Binary Black Hole Mergers**

EMILY MCPIKE  <sup>1,2</sup> ROSALBA PERTA  <sup>3</sup> K.E. SAAVIK FORD  <sup>1,2,4,5</sup> BARRY MCKERNAN  <sup>1,2,4,5</sup> VERA DELFAVERO  <sup>6</sup>  
HARRISON E. COOK  <sup>7</sup> MIRANDA MCCARTHY  <sup>1,2</sup> KAILA NATHANIEL  <sup>8</sup> JAKE POSTIGLIONE  <sup>1,2</sup> NICOLAS POSNER  <sup>9</sup>  
VARUN PRITMANI  <sup>2</sup> SHAWN RAY  <sup>1,2</sup> AND RICHARD O'SHAUGHNESSY  <sup>8</sup>

<sup>1</sup>Graduate Center, City University of New York, 365 5th Avenue, New York, NY 10016, USA

<sup>2</sup>Department of Astrophysics, American Museum of Natural History, New York, NY 10024, USA

<sup>3</sup>Department of Physics and Astronomy, Stony Brook University, Stony Brook, NY, 11794, USA

<sup>4</sup>Department of Science, BMCC, City University of New York, New York, NY 10007, USA

<sup>5</sup>Center for Computational Astrophysics, Flatiron Institute, 162 5th Ave, New York, NY 10010, USA

<sup>6</sup>Canadian Institute for Theoretical Astrophysics, University of Toronto, 60 St George St, Toronto, ON M5S 3H8, Canada

<sup>7</sup>New Mexico State University, Department of Astronomy, PO Box 30001 MSC 4500, Las Cruces, NM 88003, USA

<sup>8</sup>Center for Computational Relativity and Gravitation, Rochester Institute of Technology, Rochester, New York 14623, USA

<sup>9</sup>Data Science Institute, University of Chicago, 5801 S Ellis Ave, Chicago, IL 60637, USA

(Dated: February 5, 2026)

## ABSTRACT

The accretion disks of active galactic nuclei (AGN) are promising environments for producing binary black hole (BBH) mergers, which have been detected via gravitational waves (GW) with LIGO-Virgo-KAGRA (LVK). BBH mergers embedded in AGN disks are unique among GW formation channels in their generic ability to produce electromagnetic (EM) counterparts, via interactions between the merger remnant and the surrounding disk gas (though these are not always observable). While such mergers represent valuable multi-messenger sources, the lack of predictive statistical models in existing literature currently limits our ability to select possible EM counterparts with GW detections in archival data and in real time using time-domain surveys such as ZTF or LSST. Here, we employ the Monte Carlo For AGN Channel Testing and Simulation code (McFACTS<sup>a</sup>) to predict the bolometric luminosities of jets and shocks associated with LVK-detectable BBH merger remnants in AGN disks. McFACTS predicts the distribution of GW observables for an underlying BH population and disk model. In this work we present a new capability that simultaneously generates the distribution of bolometric EM luminosities corresponding to these predicted GW detections. We show that (i) migration traps in dense, Sirko-Goodman-like AGN disks efficiently drive hierarchical BH mergers, yielding high-mass, high-spin BH remnants capable of powering observable EM counterparts across merger generations; and ii) mergers embedded in sufficiently dense disks with chirp mass  $\mathcal{M} \gtrsim 40M_{\odot}$  are highly likely to yield observable EM counterparts for sufficiently long-lived disks and top-heavy BH initial mass functions.

**Keywords:** Gravitational wave sources (677) – Active galactic nuclei (16) – Black hole physics (159) – High energy astrophysics (739) – Time domain astronomy (2109) – Transient sources (1851) – Jets (870)

## 1. INTRODUCTION

As the LIGO-Virgo-KAGRA (LVK) detector network (E. Capote et al. 2025; S. Soni et al. 2025; F. Acernese et al. 2023; T. Akutsu et al. 2020; The LIGO Scien-

tific Collaboration et al. 2025a) continues to frequently detect binary black hole (BBH) mergers, active galactic nuclei (AGN) remain important environments to study as an efficient channel for BBH formation and merger. Stellar mass black holes (BHs) from an active galaxies' nuclear star cluster (NSC) can be orbitally coincident with the AGN accretion disk, or captured by the AGN disk due to gas dampening and dynamical cooling (K. E. S. Ford & B. McKernan (2025), for a review). Mi-

Corresponding author: Emily McPike

Email: mcpike.ej@gmail.com

<sup>a</sup> <https://www.github.com/mcfacts/mcfacts>

gration in the disk can promote regions of higher number densities of sBHs, promoting the formation of BBHs within the disk (A. Secunda et al. 2020). The relatively high escape velocity,  $v_{\text{esc}} = \mathcal{O}(10^4 \text{ km s}^{-1}(a/10^3 R_g))$ , ( $R_g = GM_{\text{SMBH}}/c$ ) where  $a$  is the semi-major axis, imposed by the central supermassive black hole (SMBH) makes exiting the disk post-merger difficult, even with relatively strong GW recoil kick velocities imparted after merger ( $v_{\text{kick}} \leq \mathcal{O}(10^3 \text{ km s}^{-1}(a/10^3 R_g))$ , see S. Ray et al. 2026, in preparation). Therefore, the disk can retain the embedded population. Combined, these effects facilitate efficient hierarchical mergers in the disk which can be detected in gravitational waves (B. McKernan et al. 2014; I. Bartos et al. 2017; N. C. Stone et al. 2017; K. E. S. Ford & B. McKernan 2025). Repeated mergers produce a population of high mass, and, notably, high spin BHs with spins increasingly aligned with the disk and with each other with increasing generation of merger (B. McKernan & K. E. S. Ford 2024). Mergers that happen within this environment constitute the AGN channel (see H. Tagawa et al. 2020; B. McKernan et al. 2018; K. E. S. Ford & B. McKernan 2022; A. Vajpeyi et al. 2022; C. Rowan et al. 2023; G. Fabj & J. Samsing 2024; M. P. Vaccaro et al. 2024; S. H. W. Leong & J. Calderón Bustillo 2025; I. Bartos & Z. Haiman 2026; Y.-J. Li et al. 2025, and many others for studies which have constrained properties of the AGN channel).

The most recent observing run has substantially increased the GW census. The most recent LVK catalog update, GWTC-4 (The LIGO Scientific Collaboration et al. 2025a), includes the most massive merger event ever detected by LVK (The LIGO Scientific Collaboration et al. 2025b). Analysis of this census suggests a population of aligned spin mergers (Y.-J. Li et al. 2025). A census including massive and aligned-spin mergers can be well explained by hierarchical merger scenarios, including the AGN channel (V. Delfavero et al. 2025a). The AGN disk channel produces a subpopulation of events with distinctive properties – asymmetric binaries; high mass, high-spin aligned binaries – and this characteristic signature can be used to disentangle the AGN disk contribution to the census (A. Vajpeyi et al. 2022; L.-G. Zhu & X. Chen 2025); these and similar preliminary analyses provide increasing evidence this fraction is nonzero. However, the exact fraction of such events ( $f_{\text{BBH,AGN}}$ ) remains an open question. If AGN disks are commonly geometrically thin, dense and of moderate radial size ( $\lesssim 0.1\text{pc}$ ) and lifetime ( $\lesssim \text{Myr}$ ), estimates span  $f_{\text{BBH,AGN}} \sim 5 - 80\%$  (e.g. K. E. S. Ford & B. McKernan 2022; L.-G. Zhu & X. Chen 2025). Although, if AGN disks are mostly very small radially ( $\lesssim 0.01\text{pc}$ ), or very low density and geometrically thick,  $f_{\text{BBH,AGN}}$  could be

very small (Y. Tomar et al. 2026). Merger components and remnant characteristics have been studied in association with various BBH formation channels (see M. Mapelli 2021, for a review). For the AGN channel, given the AGN accretion disk is gas-rich, the embedded BHs must interact with the surrounding disk gas. Angular momentum transfer via gas torques from the disk can align and increase the spin of embedded BHs via accretion and mergers (K. E. S. Ford & B. McKernan 2025). Gas transfers angular momentum via accretion onto embedded BHs (I. Bartos & Z. Haiman 2026). Repeated mergers in AGN disks can make intermediate mass BHs (IMBHs:  $M > 10^2 M_{\odot}$ ) and if the repeated mergers occur prograde in the same plane, can also boost the merged BH spin to high values ( $\chi \sim 0.7 - 0.95$ ) depending on merger generation (B. McKernan et al. 2025; V. Delfavero et al. 2025a). It is important to acknowledge other channels of BBH formation can also produce high mass mergers: e.g. in the isolated binary scenario (K. Belczynski et al. 2010; S. E. de Mink & I. Mandel 2016) or via multiple mergers in stellar clusters (e.g., contributions from NSCs, globular clusters, C. L. Rodriguez et al. 2016; J. Hong et al. 2018; K. Kritos et al. 2023; C. S. Ye & M. Fishbach 2024) although merged BH spins in dynamical, gas-free environments are likely capped at (dimensionless spin parameter)  $\chi \sim 0.8$  (K. Kritos et al. 2023).

The AGN channel is the only BBH production pathway where mergers *always* occur within a gas-rich environment and can thus easily produce EM counterparts. Post-merger, a remnant BH interacts with surrounding AGN disk gas. Rapid accretion onto embedded remnants can produce potentially luminous electromagnetic counterparts to GW (M. J. Graham et al. 2020; H. Tagawa et al. 2023a; K. Chen & Z.-G. Dai 2023). Two main luminosity generating mechanisms have been proposed: (1) the change in orbit from the gravitational wave (GW) recoil kick imparted to the remnant at merger will dissipate energy into the disk over time and potentially generate luminous shocks (B. McKernan et al. 2019); (2) the kicked remnant rapidly accretes gas from the disk, which, when combined with a high spin ( $\chi \sim 0.5 - 0.9$ ), could trigger the remnant BH to drive a jet (e.g. M. J. Graham et al. 2020). Thermal and non-thermal emission from jets produced by BH remnants have been proposed to be observable in UV/optical and X-ray/gamma ray radiation (H. Tagawa et al. 2023a; J. C. Rodríguez-Ramírez et al. 2025; K. Chen & Z.-G. Dai 2023; H.-H. Zhang et al. 2024). Semi-analytic models have been constructed to study both the thermal and non-thermal emission for conditions expected for embedded BH remnants (H. Tagawa et al. 2024; K. Chen

& Z.-G. Dai 2025). Such models reproduce observations of candidate GW counterparts by assuming remnants can attain various accretion rates up to fifteen times the Bondi-Hoyle-Lyttleton mass accretion rate ( $\dot{M}_{\text{Bondi}}$ ) (e.g. H. Tagawa et al. 2023a), although recent GRMHD simulations of embedded BH in AGN disks suggest a limiting accretion rate of  $\sim 0.1\dot{M}_{\text{Bondi}}$  (A. J. Dittmann et al. 2024).

However, there are challenges to effectively observe potential EM counterparts to BBH mergers. AGN (here spanning Seyfert AGN and quasars) are bright ( $L_{\text{AGN}} \sim 10^{42-47} \text{ erg s}^{-1}$ ) and variable (M.-H. Ulrich et al. 1997). The driving mechanisms behind AGN variability (e.g. turbulence, magneto-rotational instability, coronal heating, variable accretion rates; O. Blaes et al. 2025; S. Hagen et al. 2024; Y.-F. Jiang et al. 2019) remain poorly constrained. Thus, the false positives in AGN lightcurves for EM counterparts to BBH mergers are poorly understood. Even if a sufficiently luminous EM counterpart is produced, an optically thick disk could prevent counterpart emission from escaping the disk rapidly, making it effectively undetectable by the time it reaches the disk photosphere. Even in the subset of cases where counterpart emission is able to escape the disk promptly (such as in the case of jet breakout), the flare might be dim and indistinguishable from a bright, variable AGN disk.

The best case scenario is one in which the emission promptly escapes the disk and outshines the AGN. However, assuming Type I AGN are approximately face-on to our line of sight and Type II AGN are approximately edge on, with roughly even numbers of each, then a reasonable rule of thumb is that breakout signatures in Type II AGN are not detectable; further, up to half the breakout signatures in Type I AGN may be undetectable, if, e.g. breakout occurs on a single side of the disk (and roughly half the time breakout will be on the opposite side to the observer). Thus, geometrically only  $\mathcal{O}(1/4)$  of all breakout EM signatures are *in principle* detectable.

Actually following up GW signatures in the EM poses an additional problem. Poor localization of the GW signal on the sky and in redshift ( $z$ ) by LVK poses yet another obstacle to observing EM counterparts. Large LVK error volumes can prevent effective EM follow up to GW events given the large number of AGNs on such extended regions of the sky. We hope that the very recent release of  $\mathcal{M}_{\text{chirp}}$  bins by LVK will help with EM follow-up in the proposed observing run later in 2026.

Despite observational challenges, efforts are being made, both archivally (e.g. V. Connaughton et al. 2016; M. J. Graham et al. 2020, 2023) and in real time (e.g.

T. Cabrera et al. 2025), to search for EM counterparts to LVK-detected BBH mergers. Surveys for EM counterparts have proposed candidates that coincide with a selection of GW events across wavelengths ranging from optical through gamma rays, including for S241125n, GW190521, and GW231123 (S.-R. Zhang et al. 2025; R. Abbott et al. 2020; M. J. Graham et al. 2020; The LIGO Scientific Collaboration et al. 2025b; L. He et al. 2025). Unfortunately, due to uncertainty about the physical processes underlying AGN variability (e.g. O. Blaes et al. 2025) and possible counterparts (e.g. H. Tagawa et al. 2023b), confident associations between GW and EM events remain elusive (e.g. concerns raised by A. Palmese et al. 2021; N. Veronesi et al. 2025). Nevertheless, several groups have made substantial efforts to find plausible counterparts and make or refute associations on a statistical basis. T. Cabrera et al. (2025) conducted statistical analyses of AGN channel-like mergers in LVK and has proposed only  $\sim 3\%$  of these GW detections have real, observed EM counterparts at a 90% confidence interval. With this limited empirical sample size, clearer studies of the correlations between expected GW and EM parameters, especially those based on detailed, physically motivated emission models for EM counterparts with anticipated timescales of emission, are therefore highly desirable and will provide important guidance for current and future followup campaigns.

The payoff for successfully observing EM counterparts to BBH mergers in AGN is significant. Multi-messenger counterparts are crucial to strongly and independently constraining  $H_0$ . With a confident EM counterpart to a BBH merger, a redshift measurement from the flare combined with the luminosity distance from the GW can provide a direct constraint on  $H_0$  (e.g. S. Nissinne et al. 2013; A. Palmese & S. Mastrogianni 2025, for a review). Efforts have been made both to bolster the statistical connection between proposed flares as well as to constrain  $H_0$  with current proposed catalogs of putative EM counterparts (T. Cabrera et al. 2025). These studies have reported  $H_0$  to an accuracy of  $\sim 7\%$  (A. Palmese & S. Mastrogianni 2025) and are consistent with measurements of  $H_0$  from (A. G. Riess et al. 2019; Planck Collaboration et al. 2020). In the upcoming decade, we expect to see a large increase in the statistical BBH merger sample. Therefore, while the discussed challenges and limitations reduce the number of potentially observable flares, it is essential to model EM counterparts to BBH mergers to better our EM follow-up methods in anticipation of the future wealth of data.

There has yet to be a fine-tunable population synthesis model for these LVK AGN channel EM counterpart

events available for testing emission models. Here, we present the first population synthesis study of EM counterparts to AGN channel BBHs. More specifically, this work introduces new capabilities in McFACTS (B. McKernan et al. 2025; H. E. Cook et al. 2025; V. Delfavero et al. 2025b) to self-consistently generate the distributions of the bolometric jet and shock luminosities as EM counterparts to LVK-detectable GW events produced by BBH mergers in the AGN channel. These results also provide constraints on the merger properties and characteristic timescales expected for BBH in AGN environments.

## 2. McFACTS V.0.4.0

McFACTS is a 1D, open-source rapid population synthesis code for dynamic compact binary formation channel in AGN disks (B. McKernan et al. 2025; H. E. Cook et al. 2025; V. Delfavero et al. 2025b) (hereafter Papers I,II,III). Here we outline the released v.0.4.0 of the McFACTS code and highlight important updates from the previously published version v.0.3.0. The reader can find full documentation at <https://github.com/mcfacts>. First, the code is now significantly faster due to improvements in code efficiency. McFACTS v.0.4.0 is much faster than v.0.3.0, with a grid of 100 AGN galaxy iterations running in 50 - 70 s on an Apple M3 (Model Identifier: Mac15,12). This test was carried out with default settings (see Tab. 1), for 70 timesteps of duration  $10^4$  yr. This is an order of magnitude improvement in the computation time over v.0.3.0.

As in Papers I, II, and III, by default we assume each galaxy has a SMBH of  $M_{\text{SMBH}} = 10^8 M_{\odot}$  which accretes at 10% of the Eddington mass accretion rate ( $\dot{M}_{\text{Edd}}$ ) yielding a bolometric AGN luminosity of  $L_{\text{AGN}} \sim 10^{45}$  erg s $^{-1}$ . We assume a Sirko-Goodman (E. Sirko & J. Goodman 2003) disk model and make use of the pAGN package (D. Gangardt et al. 2024) to interpolate over the disk. We assume that the disk lives for 0.7 Myr, has a viscosity parameter  $\alpha = 0.01$ , and spans radii [6, 50, 000]  $r_g$ .

Most of the default model assumptions of Paper I still apply (see that Paper for detailed discussion of model choices). We have improved overall code performance compared to v.0.3.0, including a bug fix to our initial eccentricity prescription, which circularized orbits more slowly than it should have. As a result, we have changed default values of `disk_bh_orb_ecc_max_init` from 0.3 to 0.9 and `timestep_num` from 50 to 70 respectively (see Table 1), allowing for a more dynamically excited initial BH population on average over a slightly longer default disk lifetime (0.7Myr). Also new in v.0.4.0, we now evolve the spin vectors for the primary and secondary

**Table 1.** Fiducial model parameters for the SMBH, AGN disk and NSC in `param/sg_default.ini`.

Parameter	Default value	Units
<code>smbh.mass</code>	$10^8$	$M_{\odot}$
<code>disk_model_name</code>	<code>sirko_goodman</code>	
<code>flag_use_pagn</code>	1	
<code>flag_use_surrogate</code>	-1	
<code>flag_use_spin_check</code>	0	
<code>flag_phenom_turb</code>	0	
<code>phenom_turb_centroid</code>	0	
<code>phenom_turb_std_dev</code>	1.0	
<code>disk_radius_trap</code>	700	$r_g, \text{SMBH}$
<code>disk.radius_outer</code>	$5 \times 10^4$	$r_g, \text{SMBH}$
<code>disk.radius_max_pc</code>	0	
<code>disk.alpha.viscosity</code>	0.01	
<code>inner_disk_outer_radius</code>	50	$r_g, \text{SMBH}$
<code>disk.inner_stable_circ_orb</code>	6	$r_g, \text{SMBH}$
<code>disk.aspect_ratio_avg</code>	0.03	
<code>nscl.radius_outer</code>	5	pc
<code>nscl.radius_crit</code>	0.25	pc
<code>nscl.mass</code>	$3 \times 10^7$	$M_{\odot}$
<code>nscl_ratio_bh_num_star_num</code>	$10^{-3}$	
<code>nscl_ratio_bh_mass_star_mass</code>	10	
<code>nscl_density_index_inner</code>	1.75	
<code>nscl_density_index_outer</code>	2.5	
<code>nscl_spheroid_normalization</code>	1	
<code>nscl_imf_bh_mode</code>	10	$M_{\odot}$
<code>nscl_imf_bh_max</code>	40	$M_{\odot}$
<code>nscl_imf_powerlaw_index</code>	2	
<code>nscl_imf_bh_method</code>	default	
<code>nscl_bh_spin_dist_mu</code>	0	
<code>nscl_bh_spin_dist_sigma</code>	0.1	
<code>nscl_imf_powerlaw_index</code>	2	
<code>disk_bh_torque_condition</code>	0.1	
<code>disk_bh_eddington_ratio</code>	1.0	
<code>disk_bh_orb_ecc_max_init</code>	0.9	
<code>disk_radius_capture_outer</code>	$10^3$	$r_g, \text{SMBH}$
<code>disk_bh_pro_orb_ecc_crit</code>	0.01	
<code>mass_pile_up</code>	35	$M_{\odot}$
<code>timestep_duration_yr</code>	$10^4$	yr
<code>timestep_num</code>	70	
<code>capture_time_yr</code>	$10^5$	yr
<code>galaxy_num</code>	100	
<code>delta_energy_strong_mu</code>	0.1	
<code>delta_energy_strong_sigma</code>	0.02	
<code>fraction_bin_retro</code>	0.0	
<code>flag_thermal_feedback</code>	1	
<code>flag_orb_ecc_damping</code>	1	
<code>flag_dynamic_enc</code>	1	
<code>flag_torque_prescription</code>	paardekooper	
<code>harden_energy_delta_mu</code>	0.9	
<code>harden_energy_delta_sigma</code>	0.025	

NOTE—Star parameters are not included since stars are turned off by default in v.0.4.0.

BH in the time prior to merger using the `precession` module (D. Gerosa & M. Kesden 2016) so the treatment of the final BBH merger stage (including kicks) is more accurate. We have also added a phenomenological turbulence model to migration, which is off in default (`flag_phenom_turb = 0`), but which can be turned on by users (see §3.5 below).

### 3. METHODS

In this section we outline the mechanisms for generating radiation from interactions between a BBH remnant and the AGN disk, and introduce the models we use to compute the luminosities from these interactions, as well as the parameters we vary in the `McFACTS` code to probe the luminosity distribution of potential EM counterparts generated by the code.

#### 3.1. Shock Luminosity

A GW kick perturbs the original orbit of the binary (Y. Zlochower et al. 2011), and the velocity acquired by the remnant results from the combination of its Keplerian and kick velocities. As the remnant moves along its new orbit within the disk, gas that was previously contained within its Hill sphere is carried along and spreads into a bow-shaped structure surrounding it. The original Hill sphere gas collides with a comparable mass of accretion disk gas and we parameterize the bolometric shock luminosity,  $L_{\text{shock}} = E_{\text{shock}}/t_{\text{shock}}$  following (B. McKernan et al. 2019) where

$$t_{\text{shock}} = \mathcal{O}(6 \text{ months}) \times \left( \frac{R_{\text{H}}}{3R_g} \right) \left( \frac{v_{\text{kick}}}{100 \text{ km/s}} \right)^{-1} \quad (1)$$

is the duration of the shock, with  $v_{\text{kick}}$  is the GW kick velocity imparted to the post-merger remnant. The energy dissipated ( $E_{\text{shock}}$ ) is parameterized as

$$E_{\text{shock}} = 10^{47} \text{ erg} \left( \frac{M_{\text{H}}}{1 M_{\odot}} \right) \left( \frac{v_{\text{kick}}}{100 \text{ km/s}} \right)^2 \quad (2)$$

with  $M_{\text{H}}$  the mass of gas inside the Hill sphere of radius  $R_{\text{H}}$  so

$$L_{\text{shock}} \sim 10^{40} \text{ erg s}^{-1} \left( \frac{M_{\text{H}}}{1 M_{\odot}} \right) \left( \frac{v_{\text{kick}}}{10^2 \text{ km s}^{-1}} \right)^3 \left( \frac{R_{\text{H}}}{3R_g} \right)^{-1} \quad (3)$$

where  $M_{\text{H}} = \rho V_{\text{H}}$  is the mass of gas contained within the volume ( $V_{\text{H}}$ ) of the remnant’s Hill sphere with local average gas density  $\rho$ ,  $v_{\text{kick}}$  is the kick of the merger product and  $R_{\text{H}} = r_{\text{BH}}(M_{\text{BH}}/M_{\text{SMBH}})^{1/3}$  is the Hill sphere of the kicked BH of mass  $M_{\text{BH}}$  at AGN disk radius  $r_{\text{BH}}$ .

For each merger remnant in `McFACTS`, we estimate  $L_{\text{shock}}$  according to Eqn. 3.

#### 3.2. Jet Luminosity

Jets can be launched after BBH mergers if the circumbinary environment supplies sufficient gas for rapid post-merger accretion, enabling the remnant BH to enter a magnetically arrested disk (MAD) state (A. Tchekhovskoy et al. 2011). In such settings, gas inflow from the circumbinary disk or from fallback material that survives the coalescence can feed the remnant at near- or super-Eddington rates, promoting the accumulation and amplification of magnetic flux. The post-merger BH can then compress and advect this flux to build the large-scale poloidal magnetic field required for a Blandford–Znajek (BZ) outflow (R. D. Blandford & R. L. Znajek 1977), provided its spin is high enough to supply the necessary rotational energy. The transient accretion flow that forms immediately after the merger naturally evolves toward a MAD configuration under these conditions, allowing a relativistic jet to be launched.

Jet power ( $L_{\text{jet}}$ ) depends on the accumulation of magnetic flux onto the BH and on the efficiency of energy extraction via the BZ mechanism which we parameterize as

$$L_{\text{jet}} = \eta_{\text{jet}} \dot{M} c^2 \quad (4)$$

where the efficiency parameter  $\eta_{\text{jet}}$  depends on the BH spin as  $\propto \chi^2$  (with small corrections for high values of  $\chi$ , A. Tchekhovskoy et al. 2011) and on the strength with which magnetic flux is transported to the accreting BH via turbulent accretion. General Relativistic Magneto-Hydrodynamic (GRMHD) simulations by A. Tchekhovskoy et al. (2011) have shown  $\eta_{\text{jet}} > 1$ , implying that spinning BH yield  $L_{\text{jet}}$  with energies greater than the rest-mass energy supplied by accretion, since the jet taps the BH rotational energy.

Following the merger, the remnant BH interacts dynamically and (magneto)-hydrodynamically with surrounding disk gas.

For a BH of mass  $M_{\text{BH}}$  moving at relative velocity  $v_{\text{rel}}$  through gas of density  $\rho$  and sound speed  $c_s$ , the Bondi–Hoyle–Lyttleton (BHL) accretion rate is

$$\dot{M}_{\text{BHL}} \simeq \frac{4\pi G^2 M_{\text{BH}}^2 \rho}{(v_{\text{rel}}^2 + c_s^2)^{3/2}}, \quad (5)$$

where  $v_{\text{rel}} \sim v_{\text{kick}}$  and  $\dot{M}_{\text{BHL}}$  can greatly exceeds the Eddington limit ( $\dot{M}_{\text{Edd}}$ ) in large parts of our model disk.

While  $\dot{M}_{\text{BHL}}$  offers a useful order-of-magnitude estimate for accretion onto the remnant BH, numerous studies demonstrate that significant deviations can arise owing to various physical effects. C.-L. Jiao et al. (2025) argue that differential rotation in an AGN disk implies substantial angular momentum in the surrounding disk

gas, necessarily driving accretion via a disk-like flow rather than a Bondi-type flow with  $\dot{M} \ll \dot{M}_{\text{BHL}}$ . The accumulation of magnetic flux on horizon scales can also reduce  $\dot{M}$  (H. Cho et al. 2023). Conversely, shocks due to large  $v_{\text{rel}}$  can enhance  $\dot{M} \sim 10\dot{M}_{\text{BHL}}$  (H. Tagawa et al. 2023a).

Recent GRMHD studies of jet launching during BHL accretion find  $\dot{M} = f_{\text{acc}}\dot{M}_{\text{BHL}}$  with  $f_{\text{acc}} \approx 0.05$ , with high jet efficiency  $\eta_{\text{jet}} \approx 2 - 3$ , for BH spins of  $\chi = 0.9$  (N. Kaaz et al. 2023; Y. Kim & E. R. Most 2025). We follow these numerical results by parameterizing  $L_{\text{jet}}$  as

$$L_{\text{jet}} \sim 0.1 \left( \frac{f_{\text{acc}} \eta_{\text{jet}}}{0.1} \right) \left( \frac{\chi}{0.9} \right)^2 \dot{M}_{\text{BHL}} c^2. \quad (6)$$

and calculating this quantity for every BBH merger in McFACTS. We assume jets are launched only when  $\dot{M}_{\text{BHL}} > M_{\text{Edd}}$  (i.e. the minimal threshold for jet launching is well below  $L_{\text{AGN}}$ ). We caution that given uncertainties still inherent in the problem and our limited range of parameter study,  $L_{\text{jet}}$  used here should be considered as a guide and potentially susceptible to rescaling. Jets in N. Kaaz et al. (2023); Y. Kim & E. R. Most (2025) are sporadic with an active phase approximately to last  $\sim 24000R_g/c \sim 10^7$  s ( $M_{\text{SMBH}}/10^8M_{\odot}$ ) which we use as our fiducial jet lifetime here.

### 3.2.1. Observability of the Jet Emission

Once a jet is launched by merging BHs within an AGN disk, the detectability of its radiation remains challenging due to the extreme densities of the surrounding medium—even under the most favorable conditions of a face-on viewing angle. The most fundamental criterion for the jet’s observability is whether it can successfully break out of the disk while it is still active and radiating, thereby allowing its emission to freely escape toward the observer. In the following, we derive a simple criterion to assess whether the jet is capable of emerging from the disk.

Given a jet of luminosity  $L_{\text{jet}}$ , let  $\theta_{\text{jet}}$  be its half-opening angle and  $T_{\text{jet}}$  its duration with. Let then  $\rho$  and  $H = h/R$  the disk scale height at its location ( $R$ ). The jet can successfully emerge from the disk (“break out”) if the jet head reaches the disk surface within the engine lifetime ( $\mathcal{O}(10^7)$  s).

The jet head cross-section is approximately

$$\sigma \approx \pi(\theta_{\text{jet}} H)^2. \quad (7)$$

A convenient dimensionless measure of jet strength is then provided by the dimensionless parameter (C. D. Matzner 2003; O. Bromberg et al. 2011)

$$\tilde{L} \equiv \frac{L_{\text{jet}}}{\sigma \rho c^3} = \frac{L_{\text{jet}}}{\pi(\theta_{\text{jet}} H)^2 \rho c^3}. \quad (8)$$

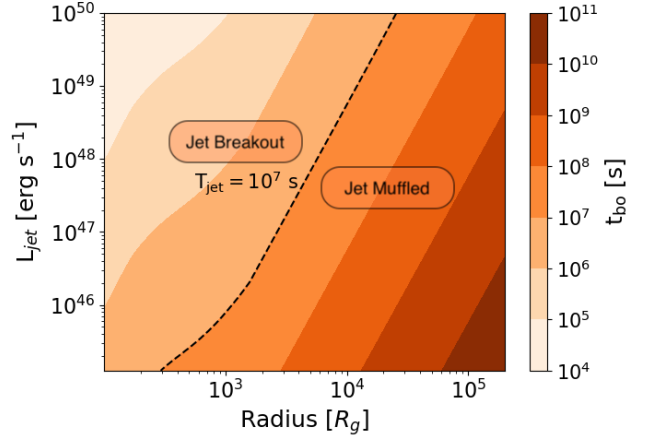


**Figure 1. Jet Breakout Time for Representative Luminosities as a Function of Remnant Location.** Regions of the disk where, for a given a luminosity, a jet is able to break out of the disk before the engine turns off ( $t_{\text{bo}} < T_{\text{jet}}$ ). Breakout times are denoted by the color bar. Our fiducial jet lifetime  $T_{\text{jet}} = 10^7$  s is annotated as a dashed black line. For our fiducial jet lifetime, any jet with a luminosity and radius lying to the left of the dotted line will breakout. Any jet whose luminosity and launching radius place it to the right of the dashed line will be muffled, escaping the disk only on the photon-diffusion timescale.

This parameter measures the ratio between the energy density of the jet and the rest-mass energy density of the surrounding medium at the jet-head location.

For a relativistic jet expanding in a non-relativistic medium with a strong reverse shock, the velocity of the jet head can then be approximated via the expression (C. D. Matzner 2003)

$$\beta_h \equiv \frac{v_h}{c} \simeq \frac{\tilde{L}^{1/2}}{1 + \tilde{L}^{1/2}}. \quad (9)$$

The breakout time  $t_{\text{bo}}$ , i.e., the time required for the jet head to traverse the vertical extent  $H$  of the disk, is then given by

$$t_{\text{bo}} \simeq \frac{H}{v_h} = \frac{H}{\beta_h c}. \quad (10)$$

If the jet head reaches the surface of the disk before the power ceases, the jet can successfully emerge from the disk. The condition for successful breakout is simply therefore:

$$T_{\text{jet}} > t_{\text{bo}} \Rightarrow \text{Jet breakout.} \quad (11)$$

If  $T_{\text{jet}} < t_{\text{bo}}$ , the jet stalls and becomes choked, depositing its energy into a hot cocoon rather than producing a directly observable relativistic outflow.

Fig. 1 shows, for our fiducial Sirko-Goodman disk model with central mass  $M = 10^8M_{\odot}$ , the regions in

the disk from which break out can occur, as a function of the duration of the active phase  $T_{\text{jet}}$ , and for a few representative values of the jet luminosity, for a reference jet angle  $\theta_{\text{jet}} = 10^\circ$ . The dashed line indicates where the jet is choked before it can emerge from the disk for an assumed jet duration  $T_{\text{jet}} = 10^7$  s. Note that this simple analysis assumes that the jet travels along the direction perpendicular to the disk plane. If it is instead oriented at some angle  $\theta_{\text{obs}}$ , the jet will have to travel a longer distance of  $H/\cos\theta_{\text{obs}}$ . This will result in slight variations for the jet breakout with respect to what is shown in Fig. 1.

If the jet fails to break out of the disk, the likelihood of detecting any emission from it before it stalls depends critically on the optical depth between the jet head and the disk photosphere. This is an inherently time-dependent problem, requiring the evolution of the jet within the surrounding medium to be tracked and depending sensitively on the jet's physical properties (see, e.g., R. Perna et al. 2021; J.-P. Zhu et al. 2021; Y.-H. Wang et al. 2022; H. D. Kang et al. 2025 for the specific case of GRB jets). Given that the characteristics of jets launched by post-merger BHs remain largely unconstrained, we adopt a conservative approach and estimate the maximum possible distance to the photosphere from the disk mid-plane. If the optical depth to Thomson scattering satisfies  $\tau \gtrsim 1$ , photons escape on the corresponding diffusive timescale,

$$t_{\text{diff}} \approx \frac{H\tau}{c}, \quad \text{where } \tau \approx n\sigma_{\text{T}}H, \quad (12)$$

$n = \rho/m_{\text{p}}$  with  $m_{\text{p}}$  the proton mass, and  $\sigma_{\text{T}}$  is the Thomson cross section. The emerging luminosity can then be estimated as

$$L_{\text{diff}} \sim L_{\text{jet}} \frac{T_{\text{jet}}}{t_{\text{diff}}} \frac{\Omega_{\text{jet}}}{4\pi}, \quad (13)$$

where  $\Omega_{\text{jet}}$  represents the solid angle within which the intrinsic emission is beamed; for small angles,  $\Omega_{\text{jet}} \simeq \pi\theta_{\text{jet}}^2$ . While we use the above equations in our Monte Carlo simulations, we note that adopting the full scale height  $H$  in Eq. 12 should be regarded as an upper limit. This choice implicitly assumes that the jet is launched from the mid-plane and that its radiation always emerges from that same location. In practice, as the jet propagates through the disk, the optical depth between the jet head and the disk photosphere decreases with time (see, e.g., R. Perna et al. 2021; M. Ray et al. 2023 for quantitative analyses).

### 3.3. Disk Lifetime

The lifetime of AGN disks ( $\tau_{\text{AGN}}$ ) is widely debated.  $\tau_{\text{AGN}}$  is thought to lie within the range of  $\sim 0.1$  Myr

to  $\mathcal{O}(10)$  Myr (e.g. K. Schawinski et al. 2015; A. King & C. Nixon 2015; P. Martini 2004). The lifetime of the disk impacts how long embedded BHs can continue the chain of hierarchical mergers. Shorter-lived disks may not allow for efficient hierarchical mergers. Longer-lived disks ( $\geq 2$  Myr) could become inefficient as well, due to consumption of the initial population of BHs (Paper III). Considering these dependences, here we adopt a default value  $\tau_{\text{AGN}} = 0.7$  Myr but also explore the effect of shorter ( $\tau_{\text{AGN}} = 0.25$  Myr), as well as longer ( $\tau_{\text{AGN}} = 1$  Myr) disk lifetimes.

### 3.4. Disk Size

The mechanism by which the outer disk is supported is largely unknown, though promising suggestions are radiation pressure by accreting BHs (S. Gilbaum & N. C. Stone 2022; M. Epstein-Martin et al. 2025) and magnetic pressure (P. F. Hopkins et al. 2024; H. J. Gerling-Dunsmore et al. 2025). It also remains unclear whether the accretion disk has a physical connection to the dusty, obscuring torus. Thus, the outer radius of the disk ( $R_{\text{outer}}$ ) remains uncertain. The disk size ( $\propto R_{\text{outer}}^2$ ), and scale height ( $H$ ) directly determine the number of orbits of compact objects and stars intersecting and captured by the AGN disk from the interacting NSC population. As  $R_{\text{outer}}$  increases, the number of captured objects rises. However, as NSCs typically have higher densities towards small radii, if  $R_{\text{outer}}$  grows too much, the average mutual separation between captured BH can increase, lowering the rate of encounters that form and merge BBH in AGN.

### 3.5. Phenomenological Disk Turbulence Prescription

The default prescription in McFACTS assumes that gas torques yield Type I migration of circularized ( $e \leq e_{\text{crit}} = 0.01$ ), embedded BHs (see Paper I). In order to test the effect of disk turbulence on migration, we recast the migration distance over a timestep as  $D(1 + \delta)$ , where  $D$  is the default Type I migration distance calculated by McFACTS, and  $\delta$  is an additional stochastic distance component drawn from a Gaussian distribution. The mean and variance of the Gaussian distribution (see Table 1) are user-defined, allowing the magnitude and directionality of turbulence-induced fluctuations to be tested. Effectively increasing the magnitude of  $\delta$  introduces a random-walk component to the standard mass-weighted Type I migration, thereby adding an increasing random component to the BBH pairings that result from migration.

### 3.6. BH Initial Mass Function Models

We test several BH initial mass function (IMF) models. By default (see Paper I) we draw BH from a Pareto

distribution function ( $P(M) \propto M^{-\gamma}$ ) spanning [10, 40]  $M_\odot$ , with a Gaussian bump centered at  $35 \pm 2.3 M_\odot$  to test/reproduce LVK observations. We set  $\gamma = 2$  by default, but also test a heavier IMF of  $\gamma = 1$ . Since mass segregation can strongly effect the BH MF we also test an IMF characterized by strong mass segregation by setting  $P(M) \propto M^{+2.5}$  (B. Rom & R. Sari 2025) spanning  $[10, 40] M_\odot$ , also tested by V. Delfavero et al. (2025a). Finally, we test a BH IMF consistent with the mass pile-up observed by LVK, drawn from a Gaussian distribution  $34 \pm 4 M_\odot$  (S. Kishore Roy et al. 2025). IMFs dominated by mass segregation have heavier BHs on average, with larger average Hill radii ( $R_H$ ) and which will migrate faster. We therefore expect the most efficient chain of hierarchical mergers to result from the mass segregated BH IMFs.

### 3.7. Initial Spin Distribution Models

The natal spin distribution of BHs is not well understood. Here we follow the default model in Papers I and II where spin magnitudes are drawn from a Gaussian centered on  $\chi = 0$ , with variance  $\sigma_\chi$ . We make use of the semi-analytical precession model outlined in D. Gerosa & M. Kesden (2016) to calculate more accurately ( $\chi, v_{\text{kick}}$ ) of remnant BHs. We change  $\sigma_\chi$  to investigate the impact on expected jet and shock luminosities.

## 4. RESULTS

In this section we present the bolometric jet and shock luminosities produced in a fiducial McFACTS v.0.4.0 simulation, their rates of likely detectability, and we examine how variations in the underlying physical parameters impact these distributions.

For convenience, if the number density of AGN is approximately  $n_{\text{AGN}} \sim 10^{-3} \text{ Mpc}^{-3} \sim 10^6 \text{ Gpc}^{-3}$  (B. McKernan et al. 2018), and if the average AGN disk lasts  $\sim 1$  Myr, a useful merger rate unit is  $\mathcal{R}_{\text{GW}} = 1$  merger/AGN/Myr, which corresponds to  $\mathcal{R}_{\text{GW}} = 1 \text{ Gpc}^{-3} \text{ yr}^{-1}$  (or  $\sim 4\%$  of the observed LVK rate) (Paper I).

### 4.1. Fiducial Model

Various results of the default/fiducial McFACTS v.0.4.0 simulation, using the parameters in Table 1, are presented in Fig. 2 through Fig. 4, with variations of the default parameters in later plots. We follow Papers I,II,III by assigning marker colors in all figures according to merger generation, where gold points correspond to first generation (1g-1g) mergers, purple points involve at least one second generation BH (2g) and red points correspond to mergers involving at least one third or higher generation BH ( $\geq 3\text{g}$ ). The horizontal dashed-dotted line corresponds to  $L_{\text{AGN}} = 1.26 \times 10^{45} \text{ erg s}^{-1}$  in plots showing the jet luminosity.

Fig. 2 (bottom left panel) shows  $L_{\text{jet}}$  as a function of merger radius. Two features are apparent.

The clump of (mostly red) points around  $10^3 R_g$  results from the migration swamp in this disk model, where migration speed decreases substantially before reaching the trap (vertical dashed line,  $R = 700r_g$ ) (see Paper I). The broader clump at larger radii is mergers in the bulk disk. Note the influence of the migration swamp encourages efficient hierarchical merging (which should be a source of high spin BH and potential jet formation). The top panel of Fig. 2 shows  $L_{\text{jet}}$  as a function of disk density and merger generation. The right-most panel of Fig. 2 shows a two-peaked distribution of  $L_{\text{jet}}$ , correspondingly mostly to the difference between mergers at the migration swamp and those in the bulk disk. The highest generation mergers (red points) typically have the highest masses and highest spins of the total population, yielding the largest  $L_{\text{jet}}$  around the migration swamp permitting kinetic jet luminosities potentially orders of magnitude greater than that of the host AGN.

From Fig. 2 the higher generation population (typically both high mass and high spin) forms most efficiently in the migration swamp at the densest and thinnest part of our disk model. Depending on the magnitude and direction of  $v_{\text{kick}}$ , BH remnants in this region, can break out of the disk on timescales ( $< T_{\text{jet}}$ ).

Fig. 3 shows breakout time ( $t_{\text{bo}}$ ) as a function of  $L_{\text{jet}}$ . The jet is able to emerge from the disk (and is therefore potentially detectable) if  $t_{\text{bo}} < T_{\text{jet}}$  (horizontal green line). Most low generation BBH mergers and most mergers in the bulk disk have  $t_{\text{bo}} > T_{\text{jet}}$ . In these cases, the energy emerges on the photon diffusion timescale ( $t_{\text{diff}} \sim 10^8 - 10^9 \text{ s}$ ) with luminosity  $< L_{\text{AGN}}$ , and will contribute to disk heating but will be indistinguishable from regular AGN variability.

By contrast, Fig. 4 shows the distribution of shock luminosities  $L_{\text{shock}}$  for our fiducial model. Only a handful of mergers have  $L_{\text{shock}}$  that might be comparable to Seyfert AGN luminosities ( $\sim 10^{42} - 10^{44} \text{ erg/s}$ ) but none approach  $L_{\text{AGN}}$  for our fiducial disk model. Nevertheless, such signatures must contribute to stochastic heating and turbulence in AGN disks.

To assess how variations in the initial population affect potentially observable flares, we next investigate how changes in McFACTS input parameters modify the predicted luminosity distribution. Since, as stated earlier, shock luminosities are found to be subdominant to the luminosity of the host AGN, for the remainder of our analysis we simply focus on how parameter variations impact the  $L_{\text{jet}}$  distribution.

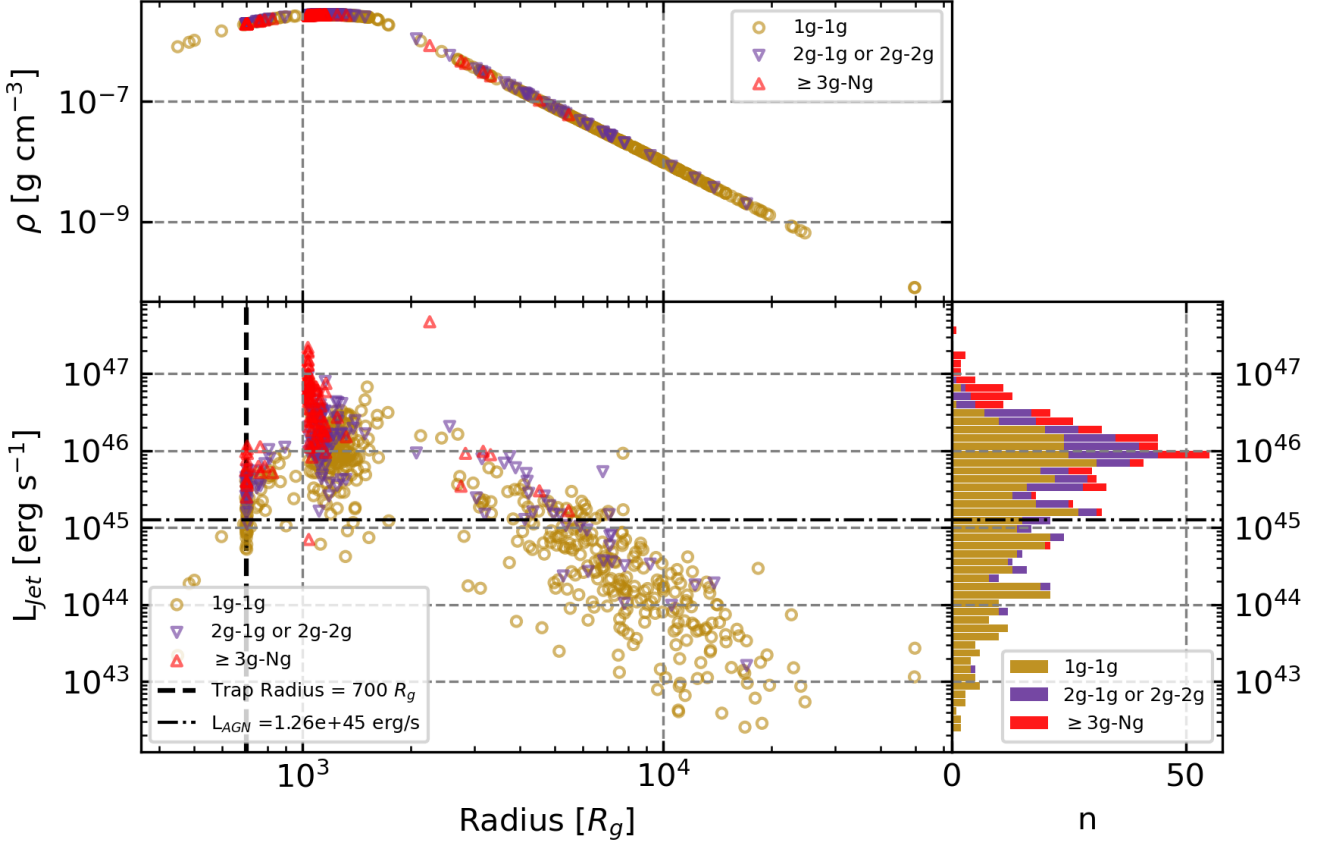


**Figure 2. Jet Luminosity as a Function of Radius in the Disk and Its Distribution in a SG Disk.** *Left panel:* Bolometric jet luminosity ( $\text{erg s}^{-1}$ ) vs. radius in disk ( $R_g$ ) calculated for each merger in McFACTS. Gold represents 1g-1g mergers, purple represents 2g- $m$ g ( $m \leq 2$ ), and red represents 3g- $n$ g ( $n \in \mathbb{Z}^+$ ), where 1g is first generation BH (never experienced a merger), 2g is second generation (previously experienced one merger), etc. *Right panel:* Number of BBH mergers per generation of BH as a function of jet luminosity. This distribution represents mergers in 100 galaxies over 0.7 Myr, with a Sirko-Goodman disk model around a  $M_{\text{SMBH}} = 10^8 M_\odot$ . The corresponding merger rate is  $\mathcal{R}_{\text{GW}} \sim 11 \text{ Gpc}^{-3} \text{ yr}^{-1}$ . The input file for this figure is `paper_em/pem_sg.default.ini` with `galaxy num = 100` and `seed = 3456789018`. (also see Paper I)

#### 4.2. Dependence on the Disk Lifetime

Here we explore how variations in the accretion disk lifetime ( $\tau_{\text{AGN}}$ ) influence the merger population and therefore the possible jet luminosities produced by embedded BBH remnants.

Fig. 5 shows the effect of varying the disk lifetime from  $\tau_{\text{AGN}} = 0.25 - 1 \text{ Myr}$ , with the default  $\tau_{\text{AGN}} = 0.7 \text{ Myr}$  in the central panel. From left to right, the corresponding runs are `sg_tagn_025Myr`, `sg_default`, and `sg_tagn_1Myr`. For a short-lived 0.25 Myr disk (left panel), the number of higher-generation (and therefore high spin) mergers is significantly reduced; these systems typically produce the brightest jet luminosities, therefore only a small number of mergers generate luminous jets. In contrast, for the slightly longer-lived disk (right panel), we find an increase in luminous mergers. The extended lifetime allows hierarchical merging to

proceed for a longer period – particularly within migration traps/swamps, where the SG trap at  $700 R_g$  reaches densities of order of  $10^{-6} \text{ g cm}^{-3}$  (see the top panel of Fig. 2) – thereby promoting the production of bright jets. Prolonged hierarchical merging yields many more higher-generation remnants with the high mass and high spin required to power significant jet luminosities.

Changing the disk lifetime affects not only the total number of mergers, but also the duration over which hierarchical merger chains can proceed. Thus, as the merger rate increases, the number of mergers capable of producing potentially bright EM counterparts grows non-linearly with disk lifetime.

#### 4.3. Dependence on the Disk Size

Next, we examine how varying the outer disk radius affects the predicted bolometric jet luminosities. We adjust  $R_{\text{outer}}$  (`disk_radius_outer` in McFACTS) to

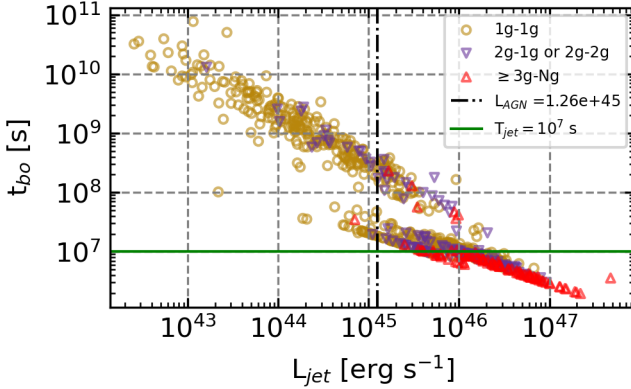


**Figure 3. Jet breakout time as a Function of Jet luminosity.** Our fiducial jet lifetime,  $T_{jet} = 10^7$  s, is indicated with a solid green line. If the breakout time is shorter than the jet lifetime, the jet is expected to break out of the disk and its emission can be potentially observable. If the breakout time is longer than the jet lifetime, then the jet emission escapes the disk on the photon diffusion time, and it is practically undetectable.

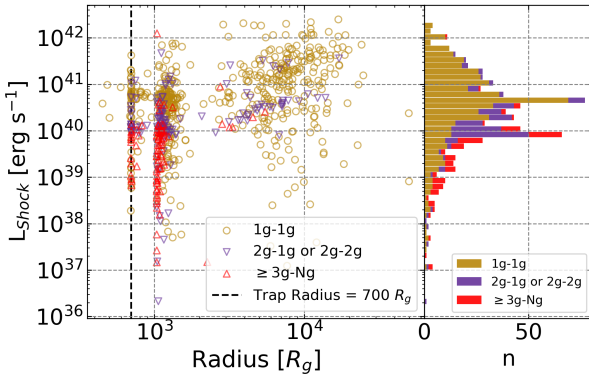


**Figure 4. Shock Luminosity as a Function of Radius in the Disk and its Distribution in the Fiducial Model.** *Left panel:* Bolometric shock luminosity ( $\text{erg s}^{-1}$ ) as a function of disk radius ( $R_g$ ) for each merger in McFACTS. *Right panel:* Number of BBH mergers per BH generation as a function of shock luminosity. This distribution corresponds to mergers occurring in 100 galaxies over 0.7 Myr, assuming a Sirko-Goodman disk model around a  $M_{\text{SMBH}} = 10^8 M_{\odot}$ . The input file for this figure is `paper_em/pem_sg_default.ini`.

a smaller value,  $2 \times 10^4 R_g$ , and to a larger value,  $7 \times 10^4 R_g$ . Changing the disk extent alters the number of initial BHs embedded in the disk and consequently modifies the resulting hierarchical merger chain.

Fig. 6 shows the results for different outer disk radii. The corresponding runs from left to right are `sg_r2e4`, `sg_default`, and `sg_r5e4`. In the first panel, corresponding to an outer disk radius of  $R_{\text{outer}} = 2 \times 10^4 R_g$ , there are fewer BBH in the outer disk than in the default run. A smaller disk radius decreases the cross section

between the NSC and the accretion disk, limiting the number of BHs that can be captured in the outer disk. However, the disk capture rate (in the inner disk) remains unchanged. As a result, the overall merger rate is lower; however, migration still drives efficient hierarchical mergers at the migration trap and swamp. With the smaller disk, a larger fraction of mergers occur at the trap, and some mergers now take place in the inner disk. Because hierarchical merging at the migration swamp and trap is not strongly suppressed, the number of potentially observable counterparts in these regions remains largely unchanged. While outer-disk mergers are reduced in this model, these events are less likely to break out.

With an extended disk (see Fig. 6 panel c) of radius  $7 \times 10^4 R_g$ , despite the larger number of initial BHs, binaries have a smaller chance to form due to the relatively larger average initial separations between BHs in the disk. As a result, the number of binaries formed is depleted and hierarchical merging is discouraged, in turn leading to a smaller number of high spin remnants. Thus, while the number of possible EM counterparts brighter than  $L_{\text{AGN}}$  is slightly depleted compared to the default run (see Fig. 6 panel b and c), the number of possible counterparts is comparable between runs.

#### 4.4. Effect of Disk Turbulence

Fig. 7 compares our fiducial run, which does not include a stochastic term, to three runs where we sequentially increase the amount of ‘turbulence’ per run. The corresponding runs from left to right are `sg_turb01`, `sg_default`, and the bottom row corresponds to runs `sg_turb1` and `sg_turb2`. In the default run (Fig. 7, panel a), the migration trap at  $700 R_g$  and the migration swamp near  $10^3 R_g$  create pile-up features as embedded BHs stall in the disk, form binaries, and merge. These BHs promote hierarchical mergers and thus faster spinning remnants. Broadly, Fig. 7 shows that the introduction of stochastic turbulence on top of migration smears out and shifts radially outwards the clump of hierarchical mergers at the migration swamp (around  $\sim 10^3 r_g$ ). Likewise, the hierarchical mergers at the migration trap are suppressed by turbulence and also smeared out. Generally, as turbulence is increased, there is a slight increase in the variance of  $L_{\text{jet}}$  as a function of a given merger radius.

#### 4.5. Dependence on the Initial Mass Function

Next, we investigate how varying the initial BH mass function affects the resulting bolometric jet luminosities. We modify the IMF to follow  $\gamma \propto M^{-1}, M^{+2.5}$  by adjusting the parameter `nsc_imf_powerlaw_index`.

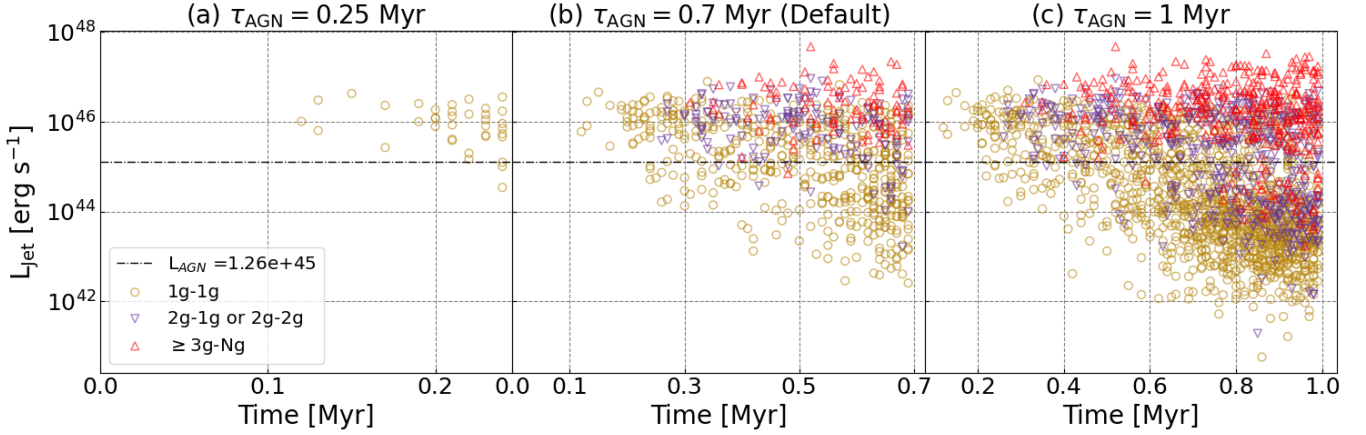


**Figure 5. Effects of The Disk Lifetime.** Bolometric jet luminosity ( $\text{erg s}^{-1}$ ) as a function of merger time (Myr), for disks with lifetimes  $\tau_{\text{AGN}} = 0.25, 0.7$ , and  $1$  Myr (left to right). The corresponding merger rates are  $\mathcal{R}_{\text{GW}} \sim 1 \text{ Gpc}^{-3}\text{yr}^{-1}$ ,  $\mathcal{R}_{\text{GW}} \sim 11 \text{ Gpc}^{-3}\text{yr}^{-1}$ , and  $\mathcal{R}_{\text{GW}} \sim 23 \text{ Gpc}^{-3}\text{yr}^{-1}$ .

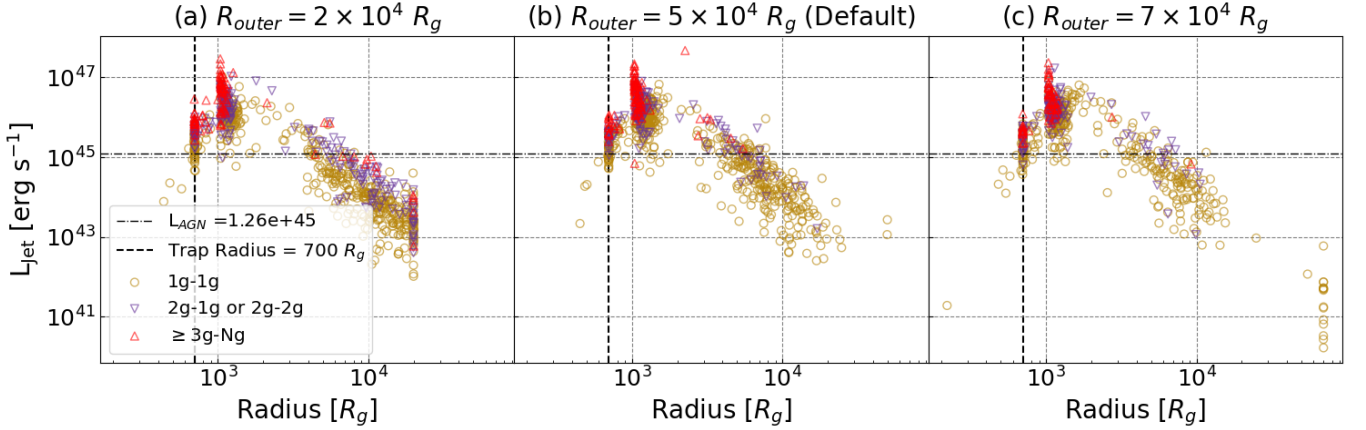


**Figure 6. Effect of the Radial Extent of the Accretion Disk.** Bolometric jet luminosity ( $\text{erg s}^{-1}$ ) as a function of radial distance ( $R_g$ ), for disks of different sizes: (from left to right)  $R_g = 2 \times 10^4 R_g$ ,  $5 \times 10^4 R_g$ ,  $7 \times 10^4 R_g$ . The corresponding merger rates are  $\mathcal{R}_{\text{GW}} \sim 11 \text{ Gpc}^{-3}\text{yr}^{-1}$ ,  $\mathcal{R}_{\text{GW}} \sim 11 \text{ Gpc}^{-3}\text{yr}^{-1}$ , and  $\mathcal{R}_{\text{GW}} \sim 8 \text{ Gpc}^{-3}\text{yr}^{-1}$ .

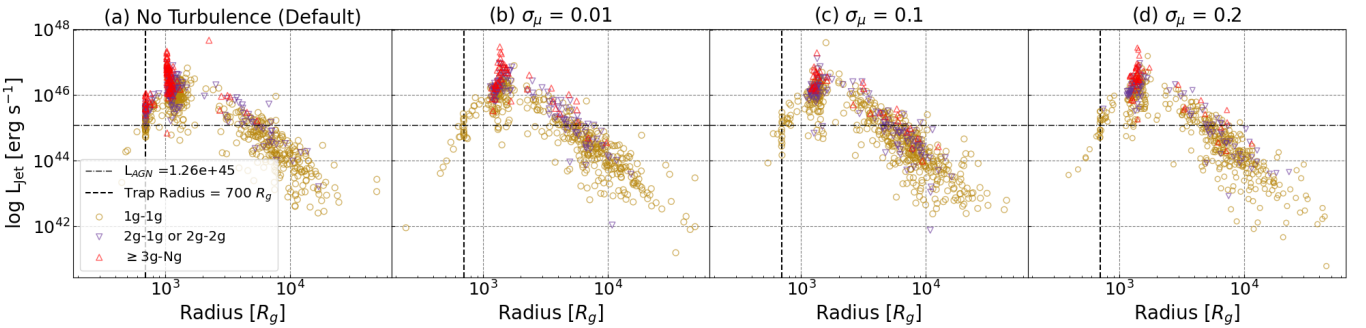


**Figure 7. Dependence on Disk Turbulence Strength.** Bolometric jet luminosity ( $\text{erg s}^{-1}$ ) as a function of radial distance ( $R_g$ ), for models in which the migration prescription includes a stochastic component to mimic disk turbulence. The width of the Gaussian governing the turbulent migration term is varied between panels. The left panel shows the fiducial model without turbulence, while the other panels correspond to progressively more turbulent disks, with  $\sigma_{\text{migration}} = 0.01, 0.1, 0.2$  (left to right). The corresponding merger rates are  $\mathcal{R}_{\text{GW}} \sim 11 \text{ Gpc}^{-3}\text{yr}^{-1}$ ,  $\mathcal{R}_{\text{GW}} \sim 8 \text{ Gpc}^{-3}\text{yr}^{-1}$ ,  $\mathcal{R}_{\text{GW}} \sim 9 \text{ Gpc}^{-3}\text{yr}^{-1}$ , and  $\mathcal{R}_{\text{GW}} \sim 8 \text{ Gpc}^{-3}\text{yr}^{-1}$ .

The results for varied BH IMF are compared in Fig. 8. The corresponding runs from left to right are `sg_default`, `sg_g1`, `sg_g25`, and `sg_gpeak`. The steep, negatively sloped IMF in our default model (Fig. 8 panel a),  $\gamma \propto M^{-2}$ , biases the initial BH masses towards lower values. Lower initial masses lengthen the timescale required to build high-mass, high-spin remnants through hierarchical mergers and result in a remnant population with a lower average mass compared to the other IMFs we explore.

With a flatter IMF of  $M^{-1}$  (Fig. 8 panel b), higher mass BHs can be initially assigned to objects embedded in the disk. This shifts the initial BH masses towards higher values, producing even more massive remnants as these BHs merge. Because McFACTS assumes a binary to form when the Hill radii of two BHs overlap, and the Hill radius scales with mass, the higher masses lead to more frequent mergers. This increased merger rate efficiently builds up BH mass and spin, thus creating a population potentially capable of driving bright jets.

The next IMF we explore has the functional form  $M^{+2.5}$ . Fig. 8 panel c shows that a steep, positively sloped IMF of  $M^{+2.5}$  biases the initial BH population towards substantially larger masses. The resulting larger Hill radii enhance the probability of binary formation, thereby promoting hierarchical mergers. This efficiently pumps up the masses and spins of the embedded population, which are key for producing bright jets. Under this steep IMF, we find that 1g mergers occur at significantly higher masses. Distinct features emerge in the 2g and  $\geq 3g$  mergers, reflecting the buildup of mass through successive mergers at the migration swamp. The lower-mass component originates in the outer disk. Last, we consider an IMF which restricts the initial masses to the  $34 \pm 4M_{\odot}$  peak observed by LVK. Fig. 8 panel d shows a top-heavy, peak-only IMF, where  $\sim 35M_{\odot} + 35M_{\odot}$  mergers dominate the first generation of BHs. As in the  $M^{+2.5}$  case, features in the 2g and  $\geq 3g$  mergers result from the buildup of mass through successive mergers at the migration swamp. Overall, the IMF strongly regulates the efficiency with which BHs grow through mergers, and as the remnant masses increase, the jet luminosities rise proportionally.

#### 4.6. Dependence on the Initial Spin Distribution

Last, we explore how altering the width of the Gaussian distribution from which the initial spins are drawn impacts the jet luminosity. By modifying the parameter `sc_bh_spin_dist_sigma` in McFACTS, we adjust the spread of the initial spin distribution and therefore the dispersion of 1g merger spins. The corresponding runs from left to right are `sg_spin_dist_sigma_02`,

`sg_default`, and `sg_spin_dist_sigma_2`. As the Gaussian is broadened (panels a through c, with width increasing left to right), the spin values of 1g mergers diffuse. The broadest distribution ( $\sigma_{\chi} = 0.2$ ) shifts the 1g merger spins to lower values, due to the initial population containing a larger spread of spins. Because the jet luminosity scales as  $\chi^2$ , this produces a corresponding reduction in jet power.

In contrast, a narrower initial distribution,  $\sigma_{\chi} = 0.02$ , yields a slightly more concentrated set of initial spins and preserve features associated with migration-trap clustering in the disk. Across all spin distributions, the impact on higher-generation spins is comparatively modest, as these remnants acquire their spins primarily through hierarchical mergers, with the dominant contribution arising from the orbital angular momentum of the binaries that formed them. In most cases, the binary orbital angular momentum is aligned with the angular momentum of the disk. Additionally, these higher generation BHs have been further spun up by accretion in the disk.

Changing the initial spin distribution in the disk has minimal impact on the overall merger rate or on the formation of higher generation remnants. Consequently, the jet luminosities from the brightest  $\geq 3g$  merger products remain essentially unchanged.

## 5. DISCUSSION: CORRELATING EM AND GW COUNTERPARTS TO BBH MERGERS

At the population level, we can identify the types of mergers most likely to produce observable EM counterparts. In our model, high-mass, high-spin BBH remnants – particularly 2g and  $\geq 3g$  mergers – are the dominant sources of significant jet luminosities.

The top panel of Fig. 10 shows the fraction of mergers with observable flares per Grace-DB<sup>10</sup> chirp mass  $\mathcal{M}$  bin, as well as the kinetic jet luminosity, remnant spin, and jet breakout time for all mergers in our fiducial model, as a function of chirp mass  $\mathcal{M}$  in subsequent panels. Fig. 10 represents the full sample of simulated mergers, with the subset of merger remnants with observable EM counterparts color-coded by merger generation, while grayed points represent muffled, unobservable points. Colored points (gold, purple, red for sequential merger generations, see discussion in Sec. 3) indicates the subset of merger remnants whose jets both breakout before the jet turns off ( $t_{\text{bo}} < T_{\text{jet}}$ ) and ex-

<sup>10</sup> <https://gracedb.ligo.org/>

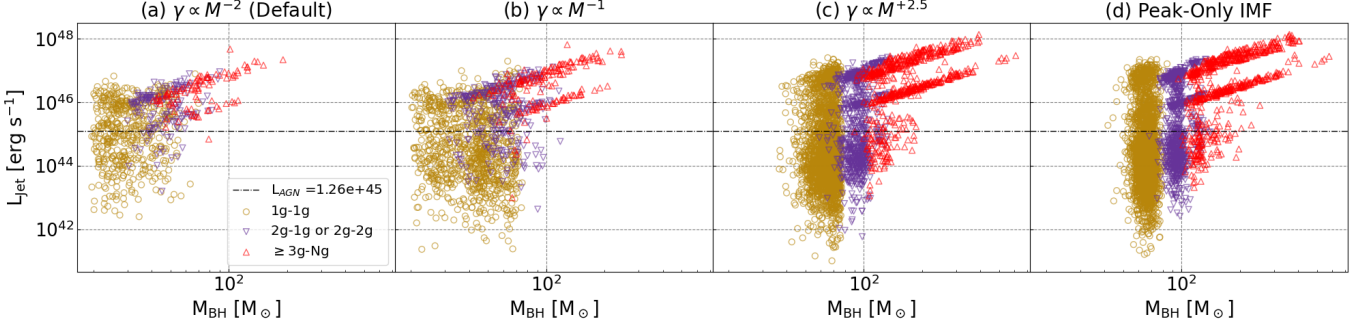


**Figure 8. Dependence of Remnant Mass on the Nuclear Star Cluster BH IMF.** Jet luminosity ( $\text{erg s}^{-1}$ ) as a function of primary mass. From left to right, the IMF is varied according to  $\gamma \propto M^{-2}, M^{-1}, M^{+2.5}$  and a peak-only power law with  $M^{-2}$ . The corresponding merger rates are  $\mathcal{R}_{\text{GW}} \sim 11 \text{ Gpc}^{-3} \text{ yr}^{-1}$ ,  $\mathcal{R}_{\text{GW}} \sim 21 \text{ Gpc}^{-3} \text{ yr}^{-1}$ ,  $\mathcal{R}_{\text{GW}} \sim 51 \text{ Gpc}^{-3} \text{ yr}^{-1}$ , and  $\mathcal{R}_{\text{GW}} \sim 54 \text{ Gpc}^{-3} \text{ yr}^{-1}$ .

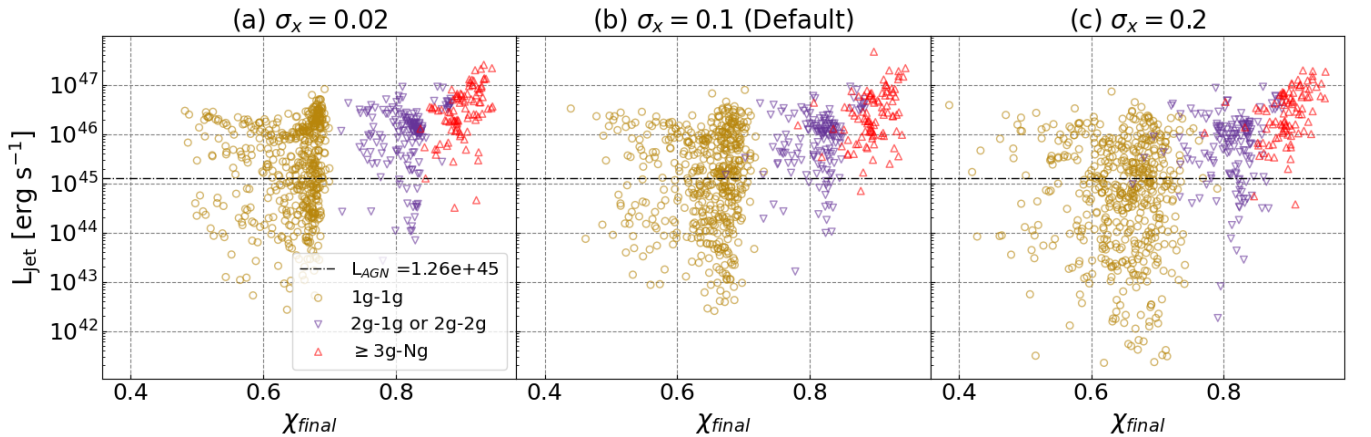


**Figure 9. Dependence on the Initial Spin Distribution.** Jet luminosity ( $\text{erg s}^{-1}$ ) as a function of BH spin. From left to right, the width of the Gaussian used to sample initial BH spins is varied to  $\sigma_x = 0.02, 1, 0.2$ . The resulting merger rates are all  $\mathcal{R}_{\text{GW}} \sim 11 \text{ Gpc}^{-3} \text{ yr}^{-1}$ .

ceed the AGN luminosity  $L_{\text{jet}} > L_{\text{AGN}}$ <sup>11</sup>. However, we note that all BHs with  $t_{\text{bo}} < T_{\text{jet}}$  also have jet luminosities  $L_{\text{jet}} > L_{\text{AGN}}$ , without a  $L_{\text{jet}} > L_{\text{AGN}}$  cut imposed. We include a point with the GW observable from GW190521 as well as the EM observables from ZTF19abanrhr ( $t_{\text{bo}}$ , where we assume the breakout time here is the rest-frame photon diffusion time, see M. J. Graham et al. 2020, for reference) the most studied EM counterpart candidate to the GW event for comparison with our model predictions.

We present two model realizations for discussion: the default model and the peak-only IMF model. Both models show the breakout time is fully consistent with our  $t_{\text{bo}}$  model (see Fig. 10, 11). The GW190521 + ZTFa-

banrhr point falls within  $2\sigma$  of the spin and jet luminosity distributions of our default model.

Fig. 10 and Fig. 11 suggest GW190521 could be the product of a 2g or 3g merger. In the peak-only scenario, we would expect a slightly higher spin value than reported, but the spin is in agreement at the  $2\sigma$  level. An assumption of larger spin has little impact on the inferred chirp mass (C. Cutler & É. E. Flanagan 1994). Additionally, because  $L_{\text{jet}}$  is lower than expected by our model, we propose the the jet could have been observed off-axis, which would explain this deficit.

Figure 12 shows the likelihood that a merger produces an observable electromagnetic counterpart, as a function of chirp mass, for each region of parameter space explored in this study. In particular, for our fiducial model, these likelihoods are  $p_{\text{EM}} \sim 16\%, 27\%, 72\%$ , and  $100\%$  for the chirp mass bins  $\mathcal{M} = [3.0M_{\odot} - 11.0M_{\odot}, 11.0M_{\odot} - 22.0M_{\odot}, 22.0M_{\odot} -$

<sup>11</sup> We remind the reader that this condition is conservative, as it assumes that the bulk of the jet's electromagnetic emission emerges in the same band as that of the AGN.

**Table 2. Rate and Percent of Mergers with Observable EM Flares Per Run.** Default model parameter values, BBH gravitational wave rate ( $\mathcal{R}_{GW}$ ), and (per cent) fraction of *all mergers* with flares ( $f_{EM} = n_{\text{flares}}/n_{\text{mergers}}$ ). Each simulation in our parameter study is listed by run name, parameter varied, and varied value, as well as resultant values of  $\mathcal{R}_{GW}$  and  $f_{EM}$ .

Run	Parameter	Value	$\mathcal{R}_{GW}$ [Gpc $^{-3}$ Myr $^{-1}$ ]	$f_{EM}$ (%)
<b>default</b>	$\tau_{\text{AGN}}$	0.7 Myr	11	33%
	$R_{\text{outer}}$	$5 \times 10^4 R_g$		
	$\sigma_\mu$	...		
	$\gamma$	$\propto M^{-2}, [10, 40] M_\odot$		
	$\sigma_\chi$	0.01		
<b>sg_tagn_025Myr</b>	$\tau_{\text{AGN}}$	0.25 Myr	1	32%
<b>sg_tagn_1Myr</b>	$\tau_{\text{AGN}}$	1 Myr	23	26%
<b>sg_r2e4</b>	$R_{\text{outer}}$	$2 \times 10^4 R_g$	11	26%
<b>sg_r7e4</b>	$R_{\text{outer}}$	$7 \times 10^4 R_g$	8	37%
<b>sg_turb01</b>	$\sigma_\mu$	0.01	8	19%
<b>sg_turb1</b>	$\sigma_\mu$	0.1	9	15%
<b>sg_turb2</b>	$\sigma_\mu$	0.2	8	19%
<b>sg_g1</b>	$\gamma$	$\propto M^{-1}, [10, 40] M_\odot$	21	33%
<b>sg_g25</b>	$\gamma$	$\propto M^{+2.5}, [10, 40] M_\odot$	51	34%
<b>sg_gpeak</b>	$\gamma$	$34 \pm 4 M_\odot$	54	32%
<b>sg_spin_dist_sigma_02</b>	$\sigma_\chi$	0.02	11	44%
<b>sg_spin_dist_sigma_2</b>	$\sigma_\chi$	0.20	11	27%

$44.0M_\odot, 44.0M_\odot - 88.0M_\odot]$ , respectively. Specifically, assuming a universe of Sirkko-Goodman like AGN disks and not accounting for geometrical observing constraints, we predict 100% of BBH mergers in AGN disks in the  $44.0M_\odot - 88.0M_\odot$  produce observable EM counterparts. Accounting for geometrical observing constraints,  $\sim 1/2$  of these EM flares will be obscured in Type 2 AGNs, thus reducing the quoted probabilities. Another  $\sim 1/2$  of these observable flares will be brighter on the side of the disk opposite to the observer if imparted with a kick opposite to the observer, particularly for mergers of lower (1g) generation, which could conservatively limit the number of practically observable events by 3/4 (1/2 from obscured AGN, at least 1/2 from viewing angle effects).

Our results broadly suggest that EM follow-ups should be prioritized for events with larger chirp mass,  $\mathcal{M} \geq 44M_\odot$ , which have the highest likelihoods of producing an observable EM counterpart, on timescales of weeks to months after the GW event. For well-localized GW detections that are likely AGN candidates, monitoring of the AGNs within the GW error volume should be conducted at  $\sim$ few days to weekly cadence to establish a robust variability baseline. Our results indicate that associated emission may emerge as late as  $\sim 4$  months post-GW. This can provide an additional upper limit to counterpart emission timescales.

If we assume that all AGN disks can be represented as our default SG model, then  $\sim 15 - 44\%$  of all AGN chan-

nel mergers could have observable EM counterparts, with specific fractions depending on the various model parameters, as detailed in Tab. 2. Generally, cases where hierarchical mergers are encouraged result in a greater number of observable EM counterparts.

While we have outlined areas of binary parameter space that promote hierarchical mergers (i.e. heavy, high-spin BHs), the specific disk model will critically regulate observable EM counterpart production. In the SG disk, there is a migration trap at the highest density region which also has a small scale height, and combined these three have the following effects: (i) efficient hierarchical mergers that build heavy, high-spin BHs, (ii) dense region provides ample gas supply onto the remnant for rapid accretion to drive a powerful jet, especially in the case of a hierarchically-formed, heavy BH ( $\mathcal{M} \gtrsim 40$ ), and (iii) a small scale height allows a powerful jet to breakout relatively quickly. Non-detection of counterparts may suggest that AGN disks are more extended and/or denser than currently modeled, or that jets in AGN disks cannot be powered for a long enough time to breakout. While we suggest longer follow-up to EM counterparts based on our results, almost simultaneous EM counterpart candidates (H. Tagawa et al. 2023a) could be explained by geometrical configurations not considered here, especially if the remnant BH is kicked toward the disk photosphere and thus any jet can more promptly emerge.

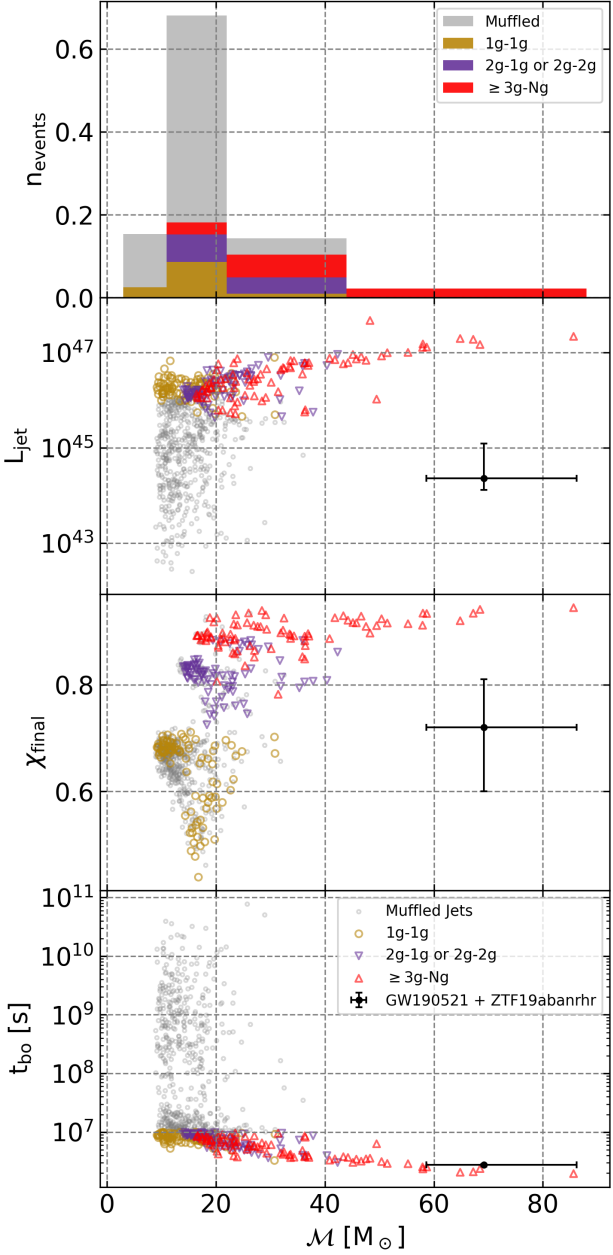


**Figure 10.** Jet Luminosity, Remnant Spin, Breakout Time and Fraction of EM Bright/Dark Mergers as a Function of Chirp Mass for the Fiducial Model. Gray points represent muffled jets and are unobservable. Colored points indicate mergers with  $L_{\text{jet}} > L_{\text{AGN}}$  and  $t_{\text{bo}} < T_{\text{jet}}$  for our fiducial  $T_{\text{jet}} = 10^7$  s. *Top panel:* Colored histograms indicate the relative fraction of mergers expected to have observable jet emission, for each generation of merger. The fraction of events with choked jets is represented by the gray histogram.

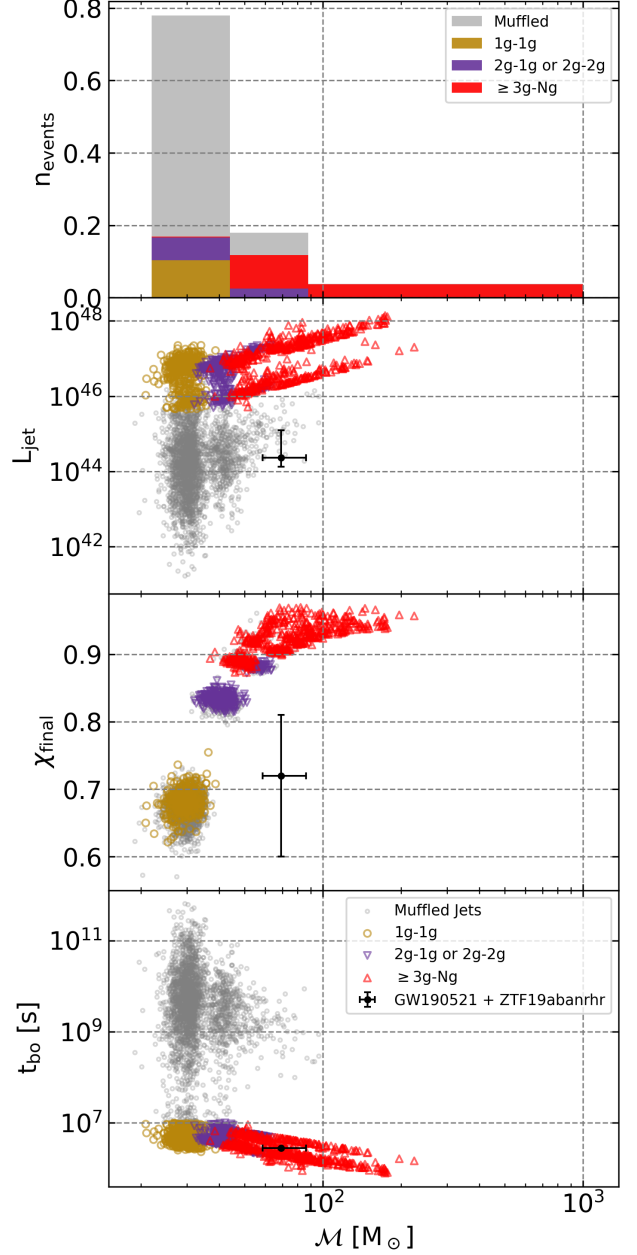


**Figure 11.** Jet Luminosity, Remnant Spin, Breakout Time and Fraction of EM Bright/Dark Mergers as a function of Chirp Mass for the peak-only IMF.

Because of the dependencies on the disk model, the detection or non-detection of EM counterparts in the upcoming eras of LISA, Cosmic Explorer, and Einstein Telescope will illuminate currently unconstrained elements of the AGN disk environment. LISA will be able to detect heavy extreme mass ratio inspirals (EMRIs) and light intermediate mass ratio inspirals (IMRIs). Top heavy BH IMFs explored here efficiently build IMBHs, which are practically guaranteed to produce EM coun-

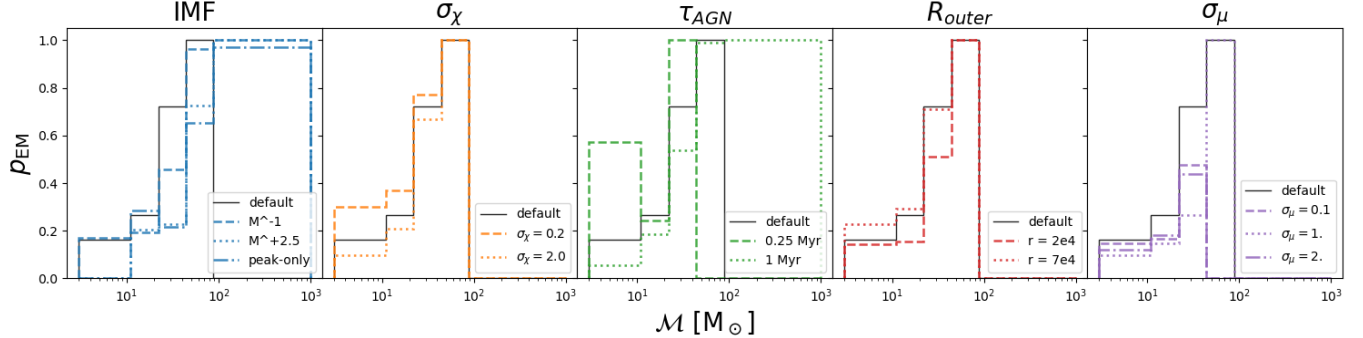


**Figure 12. Normalized Likelihood of Producing an Observable EM Counterpart as a Function of Chirp Mass.** For each model parameter explored, we compute the likelihood that a merger produces an observable EM flare within each Grace-DB-like chirp-mass bin. Results are shown in separate panels for each varied parameter (from left to right: BH IMF, spin distribution  $\sigma_\chi$ , disk lifetime  $\tau_{AGN}$ , outer disk radius  $R_{outer}$ , and turbulence  $\sigma_\mu$ ). Within each panel, different model realizations are color-coded (blue, orange, green, red, purple), while different line styles (see legend) denote individual simulations. All models are compared against the default case, shown as a solid black line.  $p_{EM}$  is normalized such that the likelihood is for all observers everywhere in the universe. A useful rule of thumb for observers is that peak  $p_{EM} \sim 0.25$  since only  $\mathcal{O}(1/4)$  of EM counterparts should actually be geometrically detectable (assuming Types 1 and 2 AGN are roughly equal in number – see text).

terparts in our model (see Fig. 12). EM counterparts to these mergers are highly promising multi-messenger sources. The Cosmic Explorer and Einstein Telescopes will reveal BBH mergers to high redshifts. With these, we expect to be able to robustly estimate the relative contribution to the BBH merger rate from the AGN channel.

From a population perspective, our results identify the conditions that most strongly favor bright jets and potentially observable EM flares. A top heavy IMF, a moderately long-lived disk, and a substantial local gas reservoir all enhance the production of high-mass, high-spin remnants capable of powering luminous jets. Although dense disks enhance merger rates through gas torques, their optically thick regions may muffle jet signatures: if a jet cannot clear a cavity and promptly penetrate the disk, it may fail to break out. Thus, jet formation and successful escape are tightly regulated by the local disk environment.

In the shock-only scenario, our simulations demonstrated bolometric shock luminosities are never luminous enough to outshine our default disk model.  $L_{shock}$  can only outshine a fraction of low luminosity AGN (LLAGN) and some Seyfert AGN, especially for large  $v_{kick} \sim 10^3 \text{ km/s}$ .

Our estimates for EM counterparts also do not take into account that EM signals could be emitted closer to the photosphere of one side of the disk opposite to the observer, and that another fraction of these systems will happen in Type II/edge-on AGN. More generally, if the EM emission from the jet is highly anisotropic, then the angle between the jet axis and the observer line of sight will further play an important role towards de-

tectability of the emission. Additionally, some binaries in the disk could have an interaction with a third body that perturbs the binary orbit around the SMBH, and causes the orbit to become inclined with respect to the disk (and no longer embedded). This population (with a significant non-zero  $\chi_p$ ) could diminish the amount of observable EM counterparts if they push binaries in the migration swamp out into these disk-crossing orbits, and such binaries then merge while orbiting outside of the disk.

Even without a detailed EM emission model, our framework yields population-level constraints that identify the most optimistic conditions for observability. In the future, we plan to incorporate both thermal and non-thermal emission from jetted remnants to evaluate detectability with specific telescopes. Importantly, the energy of any observable counterpart is bounded by the jet power prescribed by our input physics, providing robust upper limits on EM emission in the case mergers always occur at the midplane<sup>12</sup>. Progenitor spin directions, spins and remnant spins can be inferred through forward modeling, helping to infer plausible jet properties from candidate EM counterparts.

We have explored key uncertainties in the AGN channel and found that the prospects for observable EM emission are primarily controlled by the IMF, the presence of migration traps (and regions of dense gas), and the AGN disk lifetime, while being relatively insensitive to the initial spin distribution and the outer disk radius. As our modeling improves, these dependencies

<sup>12</sup> We remind the reader the jet lifetime is a free parameter, and thus will limit the breakout time and observability.

will enable tighter constraints on the subset of LVK merger remnants in AGN disks capable of producing bright flares and will inform ongoing surveys for EM follow-up to GW events.

## 6. CONCLUSIONS

We have presented the first population synthesis investigation of EM counterparts to BBH mergers in the AGN channel. Using the public, open-source, and reproducible McFACTS code, we have modeled jet and shock luminosities generated by GW-detectable BBH merger remnants embedded in AGN disks. By varying the accretion-disk lifetime, turbulence, and radial extent, as well as the initial BH spin distribution and their IMF, we identify regions of parameter space that yield EM luminosities exceeding the host AGN luminosity.

Our simulations demonstrate that accretion-powered jets from remnant BHs can produce significant EM emission, whereas shock-powered emission from kicked remnants remains undetectable in Sirko-Goodman disk models surrounding a  $10^8 M_\odot$  SMBH. We find that dense, moderately-lived AGN disks, combined with top-heavy BH IMFs, produce a population of high-mass, high spin BHs through hierarchical mergers, enabling the conversion of remnant spin energy into potentially observable EM counterparts. The dominant factors governing counterpart detectability are the disk density, scale height and lifetime, as well as the efficiency of hierarchical mass and spin growth of the BHs, which determines the potential jet luminosity.

Based on these results, we recommend prioritizing EM follow-up of GW events with chirp masses  $\gtrsim 44 M_\odot$  over timescales of up to  $\sim 100$  days post-merger. Our findings provide quantitative constraints on counterpart rates and can be coupled with detailed emission models to guide future surveys such as LSST. Systematic follow-up, including well-characterized non-detections, will further help constraining AGN-disk and NSC properties. Upcoming GW catalogs from LVK O4, O5, and other future observing runs will substantially expand the sample available for EM searches, enabling increasingly stringent tests of the AGN-channel scenario.

In future work, we plan to extend the computation of the jet luminosities beyond their purely bolometric values, specifically modeling the thermal and nonthermal radiation from jets and their associated cocoon emission. We will extend this analysis to a synthetic universe, as in Paper III, in order to explore the impact of varying SMBH mass, NSC mass, and accretion-disk

model. We are currently applying these methods to generate predictions for LSST and the planned UVEX mission. These efforts will enable increasingly refined forecasts for electromagnetic follow-up of gravitational-wave events in upcoming LIGO/Virgo/Kagra observing, future ground-based GW observatories, as well as LISA and other space-based GW observatories.

## 7. DATA AVAILABILITY

McFACTS is available at <https://github.com/mcfacts>, and this work was completed with the version at git hash `ba3643f`. Data and other software required to reproduce this work will be made available upon publication

## ACKNOWLEDGMENTS

EM would like to thank the CUNY GC MS Astrophysics program and the CCA GW group for support and useful comments. EM would like to thank Phil Armitage, Tomás Cabrera, Will Farr, Carrie Filion, Keefe Mittman, and Amy Secunda for helpful conversations and feedback on this work. RP acknowledges support by NASA award 80NSSC25K7554. BM, KESF and HEC are supported by NSF AST-2206096. BM, KESF & VP are supported by NSF AST-1831415 and Simons Foundation Grant 533845. VD acknowledges support from the Natural Sciences and Engineering Research Council of Canada (NSERC) under grant RGPIN-2023-05511 and the Research Corporation for Science Advancement’s Scialog Initiative under grant #SALSST-2024-089b with support from The Brinson Foundation. ROS acknowledges support from NSF PHY-2309172 and AST-2206321. JP acknowledges support provided by Schmidt Sciences, LLC. VP acknowledges support from NASA 24-MSF24-0012. This material is based upon work supported by NSF’s LIGO Laboratory which is a major facility fully funded by the National Science Foundation.

*Facilities:* The Laser Interferometer Gravitational-Wave Observatory (LIGO), Zwicky Transient Facility (ZTF)

*Software:* `Astropy` ([Astropy Collaboration et al. 2013, 2018, 2022](#)), `matplotlib` ([J. D. Hunter 2007](#)), `McFACTS` ([B. McKernan et al. 2025](#)), `numpy` ([C. R. Harris et al. 2020](#)), `pagn` ([D. Gangardt et al. 2024](#)), `pandas` ([W. McKinney 2010](#)), `precession` ([D. Gerosa & M. Kesden 2016](#)).

## APPENDIX

## A. REPRODUCIBILITY

Table 3 contains the parameters we varied in the McFACTS code to produce the results shared in this section.

**Table 3.** Parameter choices for each run described herein. For a default run, all parameters are listed in 1. We list default values under `sg_default` and denote changed values for subsequent runs. To reproduce a specific run, locate the parameter in `model_choice.ini` and alter it to the listed value.

Run	Parameter	Value
<code>sg_tagn_025Myr</code>	<code>timestep_num</code>	25
<code>sg_tagn_1Myr</code>	<code>timestep_num</code>	100
<code>sg_r2e4</code>	<code>disk_radius_outer</code>	$2 \times 10^4$
<code>sg_r7e4</code>	<code>disk_radius_outer</code>	$7 \times 10^4$
<code>sg_turb01</code>	<code>phenom_turb_std_dev</code>	0.01
	<code>flag_phenom_turb</code>	1
<code>sg_turb1</code>	<code>phenom_turb_std_dev</code>	0.1
	<code>flag_phenom_turb</code>	1
<code>sg_turb2</code>	<code>phenom_turb_std_dev</code>	0.2
	<code>flag_phenom_turb</code>	1
<code>sg_g1</code>	<code>nsc_imf_powerlaw_index</code>	1
<code>sg_g25</code>	<code>nsc_imf_powerlaw_index</code>	2.5
	<code>nsc_imf_bh_method</code>	<code>power</code>
<code>sg_gpeak</code>	<code>nsc_imf_bh_method</code>	<code>peak</code>
<code>sg_spin_dist_sigma_02</code>	<code>nsc_bh_spin_dist_sigma</code>	0.02
<code>sg_spin_dist_sigma_2</code>	<code>nsc_bh_spin_dist_sigma</code>	0.20

NOTE—`disk_model_name` determines the disk model. The default disk model is set to `sirko_goodman`. `nsc_imf_powerlaw_index` determines the slope of the probability distribution in the Pareto distribution function we draw initial masses from (see Paper I). Default IMF slope is set to 2. `nsc_imf_bh_method` changes the method used to populate the initial masses. `flag_use_surrogate` is a choice of -1 and 0 which, respectively, turn on and off precession (V. Delfavero et al. 2025a). Our default model sets this parameter to -1, but the McFACTS code has the parameter set to 0. `disk_radius_outer` determines the outermost radius of the accretion disk. The default value is  $5 \times 10^4 R_g$ . `flag_phenom_turb` determines if the disk is considered turbulent. Default is set to 0. With `flag_phenom_turb` set to 1, we add a term to consider stochastic migration due to turbulence, `phenom_turb_std_dev`. `phenom_turb_std_dev` determines how turbulent the disk is; the default value is 0.1. `nsc_bh_spin_dist_sigma` determines the spread of the Gaussian used to draw initial BH spins from. The default value is set to 0.1. The default time step is  $10^4$  (see Paper I). `timestep_num` determines the number of time steps in a run, i.e. the lifetime of the accretion disk. Default value is 50 for an accretion disk lifetime of 0.7 Myr.

## REFERENCES

Abbott, R., Abbott, T. D., Abraham, S., et al. 2020, *PhRvL*, 125, 101102,  
doi: [10.1103/PhysRevLett.125.101102](https://doi.org/10.1103/PhysRevLett.125.101102)

Acernese, F., Agathos, M., Ain, A., & et al. 2023, *Classical and Quantum Gravity*, 40, 185006,  
doi: [10.1088/1361-6382/acd92d](https://doi.org/10.1088/1361-6382/acd92d)

Akutsu, T., Ando, M., Arai, K., & et al. 2020, *Progress of Theoretical and Experimental Physics*, 2021,  
doi: [10.1093/ptep/ptaa125](https://doi.org/10.1093/ptep/ptaa125)

Astropy Collaboration, Robitaille, T. P., Tollerud, E. J., et al. 2013, *A&A*, 558, A33,  
doi: [10.1051/0004-6361/201322068](https://doi.org/10.1051/0004-6361/201322068)

Astropy Collaboration, Price-Whelan, A. M., Sipőcz, B. M., et al. 2018, AJ, 156, 123, doi: [10.3847/1538-3881/aabc4f](https://doi.org/10.3847/1538-3881/aabc4f)

Astropy Collaboration, Price-Whelan, A. M., Lim, P. L., et al. 2022, ApJ, 935, 167, doi: [10.3847/1538-4357/ac7c74](https://doi.org/10.3847/1538-4357/ac7c74)

Bartos, I., & Haiman, Z. 2026, ApJL, 996, L44, doi: [10.3847/2041-8213/ae2bff](https://doi.org/10.3847/2041-8213/ae2bff)

Bartos, I., Kocsis, B., Haiman, Z., & Márka, S. 2017, ApJ, 835, 165, doi: [10.3847/1538-4357/835/2/165](https://doi.org/10.3847/1538-4357/835/2/165)

Belczynski, K., Bulik, T., Fryer, C. L., et al. 2010, ApJ, 714, 1217, doi: [10.1088/0004-637X/714/2/1217](https://doi.org/10.1088/0004-637X/714/2/1217)

Blaes, O., Jiang, Y.-F., Lasota, J.-P., & Lipunova, G. 2025, arXiv e-prints, arXiv:2505.04402, doi: [10.48550/arXiv.2505.04402](https://doi.org/10.48550/arXiv.2505.04402)

Blandford, R. D., & Znajek, R. L. 1977, MNRAS, 179, 433, doi: [10.1093/mnras/179.3.433](https://doi.org/10.1093/mnras/179.3.433)

Bromberg, O., Nakar, E., Piran, T., & Sari, R. 2011, ApJ, 740, 100, doi: [10.1088/0004-637X/740/2/100](https://doi.org/10.1088/0004-637X/740/2/100)

Cabrera, T., Palmese, A., & Fishbach, M. 2025, arXiv e-prints, arXiv:2510.20767, doi: [10.48550/arXiv.2510.20767](https://doi.org/10.48550/arXiv.2510.20767)

Cabrera, T., Palmese, A., Hu, L., et al. 2025, Searching for electromagnetic emission in an AGN from the gravitational wave binary black hole merger candidate S230922g, arXiv, doi: [10.48550/arXiv.2407.10698](https://doi.org/10.48550/arXiv.2407.10698)

Capote, E., Jia, W., Aritomi, N., & et al. 2025, Phys. Rev. D, 111, 062002, doi: [10.1103/PhysRevD.111.062002](https://doi.org/10.1103/PhysRevD.111.062002)

Chen, K., & Dai, Z.-G. 2023, Electromagnetic Counterparts Powered by Kicked Remnants of Black Hole Binary Mergers in AGN Disks, arXiv, doi: [10.48550/arXiv.2311.10518](https://doi.org/10.48550/arXiv.2311.10518)

Chen, K., & Dai, Z.-G. 2025, Observational Properties of Thermal Emission from Relativistic Jets Embedded in AGN Disks, arXiv, doi: [10.48550/arXiv.2505.16390](https://doi.org/10.48550/arXiv.2505.16390)

Cho, H., Prather, B. S., Narayan, R., et al. 2023, ApJL, 959, L22, doi: [10.3847/2041-8213/ad1048](https://doi.org/10.3847/2041-8213/ad1048)

Connaughton, V., Burns, E., Goldstein, A., et al. 2016, ApJL, 826, L6, doi: [10.3847/2041-8205/826/1/L6](https://doi.org/10.3847/2041-8205/826/1/L6)

Cook, H. E., McKernan, B., Ford, K. E. S., et al. 2025, McFACTS II: Mass Ratio–Effective Spin Relationship of Black Hole Mergers in the AGN Channel, doi: [10.3847/1538-4357/adfd56](https://doi.org/10.3847/1538-4357/adfd56)

Cutler, C., & Flanagan, É. E. 1994, PhRvD, 49, 2658, doi: [10.1103/PhysRevD.49.2658](https://doi.org/10.1103/PhysRevD.49.2658)

de Mink, S. E., & Mandel, I. 2016, MNRAS, 460, 3545, doi: [10.1093/mnras/stw1219](https://doi.org/10.1093/mnras/stw1219)

Delfavero, V., Ray, S., Cook, H. E., et al. 2025a, Prospects for the formation of GW231123 from the AGN channel, arXiv, doi: [10.48550/arXiv.2508.13412](https://doi.org/10.48550/arXiv.2508.13412)

Delfavero, V., Ford, K. E. S., McKernan, B., et al. 2025b, 989, 67, doi: [10.3847/1538-4357/ade4c1](https://doi.org/10.3847/1538-4357/ade4c1)

Dittmann, A. J., Dempsey, A. M., & Li, H. 2024, ApJ, 964, 61, doi: [10.3847/1538-4357/ad23ce](https://doi.org/10.3847/1538-4357/ad23ce)

Epstein-Martin, M., Tagawa, H., Haiman, Z., & Perna, R. 2025, MNRAS, 537, 3396, doi: [10.1093/mnras/staf237](https://doi.org/10.1093/mnras/staf237)

Fabj, G., & Samsing, J. 2024, MNRAS, 535, 3630, doi: [10.1093/mnras/stae2499](https://doi.org/10.1093/mnras/stae2499)

Ford, K. E. S., & McKernan, B. 2022, Monthly Notices of the Royal Astronomical Society, 517, 5827, doi: [10.1093/mnras/stac2861](https://doi.org/10.1093/mnras/stac2861)

Ford, K. E. S., & McKernan, B. 2025, Using gravitational waves and multi-messenger Astronomy to reverse-engineer the properties of galactic nuclei, arXiv, doi: [10.48550/arXiv.2506.08801](https://doi.org/10.48550/arXiv.2506.08801)

Gangardt, D., Trani, A. A., Bonnerot, C., & Gerosa, D. 2024, MNRAS, 530, 3689, doi: [10.1093/mnras/stae1117](https://doi.org/10.1093/mnras/stae1117)

Gerling-Dunsmore, H. J., Begelman, M. C., Simon, J. B., & Armitage, P. J. 2025, arXiv e-prints, arXiv:2508.16842, doi: [10.48550/arXiv.2508.16842](https://doi.org/10.48550/arXiv.2508.16842)

Gerosa, D., & Kesden, M. 2016, Phys. Rev. D, 93, 124066, doi: [10.1103/PhysRevD.93.124066](https://doi.org/10.1103/PhysRevD.93.124066)

Gilbaum, S., & Stone, N. C. 2022, ApJ, 928, 191, doi: [10.3847/1538-4357/ac4ded](https://doi.org/10.3847/1538-4357/ac4ded)

Graham, M. J., Ford, K. E. S., McKernan, B., et al. 2020, 124, 251102, doi: [10.1103/PhysRevLett.124.251102](https://doi.org/10.1103/PhysRevLett.124.251102)

Graham, M. J., McKernan, B., Ford, K. E. S., et al. 2023, 942, 99, doi: [10.3847/1538-4357/aca480](https://doi.org/10.3847/1538-4357/aca480)

Hagen, S., Done, C., & Edelson, R. 2024, MNRAS, 530, 4850, doi: [10.1093/mnras/stae1177](https://doi.org/10.1093/mnras/stae1177)

Harris, C. R., Millman, K. J., van der Walt, S. J., et al. 2020, Nature, 585, 357, doi: [10.1038/s41586-020-2649-2](https://doi.org/10.1038/s41586-020-2649-2)

He, L., Zhu, L.-G., Liu, Z.-Y., et al. 2025, arXiv e-prints, arXiv:2511.05144, doi: [10.48550/arXiv.2511.05144](https://doi.org/10.48550/arXiv.2511.05144)

Hong, J., Vesperini, E., Askar, A., et al. 2018, MNRAS, 480, 5645, doi: [10.1093/mnras/sty2211](https://doi.org/10.1093/mnras/sty2211)

Hopkins, P. F., Squire, J., Su, K.-Y., et al. 2024, The Open Journal of Astrophysics, 7, 19, doi: [10.21105/astro.2310.04506](https://doi.org/10.21105/astro.2310.04506)

Hunter, J. D. 2007, Computing in Science & Engineering, 9, 90, doi: [10.1109/MCSE.2007.55](https://doi.org/10.1109/MCSE.2007.55)

Jiang, Y.-F., Blaes, O., Stone, J. M., & Davis, S. W. 2019, ApJ, 885, 144, doi: [10.3847/1538-4357/ab4a00](https://doi.org/10.3847/1538-4357/ab4a00)

Jiao, C.-L., Zhu, L., Zhao, E.-g., & Zhang, J. 2025, MNRAS, 544, 2024, doi: [10.1093/mnras/staf1899](https://doi.org/10.1093/mnras/staf1899)

Kaaz, N., Murguia-Berthier, A., Chatterjee, K., Liska, M. T. P., & Tchekhovskoy, A. 2023, ApJ, 950, 31, doi: [10.3847/1538-4357/acc7a1](https://doi.org/10.3847/1538-4357/acc7a1)

Kang, H. D., Perna, R., Lazzati, D., & Wang, Y.-H. 2025, The Open Journal of Astrophysics, 8, 23, doi: [10.33232/001c.131902](https://doi.org/10.33232/001c.131902)

Kim, Y., & Most, E. R. 2025, 111, 083025, doi: [10.1103/PhysRevD.111.083025](https://doi.org/10.1103/PhysRevD.111.083025)

King, A., & Nixon, C. 2015, MNRAS, 453, L46, doi: [10.1093/mnrasl/slv098](https://doi.org/10.1093/mnrasl/slv098)

Kishore Roy, S., van Son, L. A. C., & Farr, W. M. 2025, Classical and Quantum Gravity, 42, 225008, doi: [10.1088/1361-6382/ae1921](https://doi.org/10.1088/1361-6382/ae1921)

Kritos, K., Berti, E., & Silk, J. 2023, PhRvD, 108, 083012, doi: [10.1103/PhysRevD.108.083012](https://doi.org/10.1103/PhysRevD.108.083012)

Leong, S. H. W., & Calderón Bustillo, J. 2025, arXiv e-prints, arXiv:2512.08382, doi: [10.48550/arXiv.2512.08382](https://doi.org/10.48550/arXiv.2512.08382)

Li, Y.-J., Wang, Y.-Z., Tang, S.-P., & Fan, Y.-Z. 2025, Aligned Hierarchical Black Hole Mergers in AGN disks revealed by GWTC-4, arXiv, doi: [10.48550/arXiv.2509.23897](https://doi.org/10.48550/arXiv.2509.23897)

Mapelli, M. 2021, in Handbook of Gravitational Wave Astronomy, ed. C. Bambi, S. Katsanevas, & K. D. Kokkotas, 16, doi: [10.1007/978-981-15-4702-7\\_16-1](https://doi.org/10.1007/978-981-15-4702-7_16-1)

Martini, P. 2004, in Coevolution of Black Holes and Galaxies, ed. L. C. Ho, 169, doi: [10.48550/arXiv.astro-ph/0304009](https://doi.org/10.48550/arXiv.astro-ph/0304009)

Matzner, C. D. 2003, MNRAS, 345, 575, doi: [10.1046/j.1365-8711.2003.06969.x](https://doi.org/10.1046/j.1365-8711.2003.06969.x)

McKernan, B., & Ford, K. E. S. 2024, MNRAS, 531, 3479, doi: [10.1093/mnras/stae1351](https://doi.org/10.1093/mnras/stae1351)

McKernan, B., Ford, K. E. S., Kocsis, B., Lyra, W., & Winter, L. M. 2014, MNRAS, 441, 900, doi: [10.1093/mnras/stu553](https://doi.org/10.1093/mnras/stu553)

McKernan, B., Saavik Ford, K. E., Bellovary, J., et al. 2018, The Astrophysical Journal, 866, 66, doi: [10.3847/1538-4357/aadae5](https://doi.org/10.3847/1538-4357/aadae5)

McKernan, B., Ford, K. E. S., Bartos, I., et al. 2019, 884, L50, doi: [10.3847/2041-8213/ab4886](https://doi.org/10.3847/2041-8213/ab4886)

McKernan, B., Ford, K. E. S., Cook, H. E., et al. 2025, McFACTS I: Testing the LVK AGN channel with Monte Carlo For AGN Channel Testing & Simulation (McFACTS), arXiv, doi: [10.48550/arXiv.2410.16515](https://doi.org/10.48550/arXiv.2410.16515)

McKinney, W. 2010, in Proceedings of the 9th Python in Science Conference, ed. S. van der Walt & J. Millman, 51 – 56

Nissanke, S., Holz, D. E., Dalal, N., et al. 2013, arXiv e-prints, arXiv:1307.2638, doi: [10.48550/arXiv.1307.2638](https://doi.org/10.48550/arXiv.1307.2638)

Palmese, A., Fishbach, M., Burke, C. J., Annis, J., & Liu, X. 2021, ApJL, 914, L34, doi: [10.3847/2041-8213/ac0883](https://doi.org/10.3847/2041-8213/ac0883)

Palmese, A., & Mastrogiovanni, S. 2025, arXiv e-prints, arXiv:2502.00239, doi: [10.48550/arXiv.2502.00239](https://doi.org/10.48550/arXiv.2502.00239)

Perna, R., Lazzati, D., & Cantiello, M. 2021, ApJL, 906, L7, doi: [10.3847/2041-8213/ab319](https://doi.org/10.3847/2041-8213/ab319)

Planck Collaboration, Aghanim, N., Akrami, Y., et al. 2020, A&A, 641, A6, doi: [10.1051/0004-6361/201833910](https://doi.org/10.1051/0004-6361/201833910)

Ray, M., Lazzati, D., & Perna, R. 2023, MNRAS, 521, 4233, doi: [10.1093/mnras/stad816](https://doi.org/10.1093/mnras/stad816)

Riess, A. G., Casertano, S., Yuan, W., Macri, L. M., & Scolnic, D. 2019, ApJ, 876, 85, doi: [10.3847/1538-4357/ab1422](https://doi.org/10.3847/1538-4357/ab1422)

Rodriguez, C. L., Chatterjee, S., & Rasio, F. A. 2016, PhRvD, 93, 084029, doi: [10.1103/PhysRevD.93.084029](https://doi.org/10.1103/PhysRevD.93.084029)

Rodríguez-Ramírez, J. C., Nemmen, R., & Bom, C. R. 2025, Optical and UV Flares from Binary Black Hole Mergers in Active Galactic Nuclei, arXiv, doi: [10.48550/arXiv.2407.09945](https://doi.org/10.48550/arXiv.2407.09945)

Rom, B., & Sari, R. 2025, Segregation in Nuclear Stellar Clusters: Rates and Mass Distributions of TDEs, QPEs, Plunges, and EMRIs, <https://arxiv.org/abs/2502.13209>

Rowan, C., Boekholt, T., Kocsis, B., & Haiman, Z. 2023, MNRAS, 524, 2770, doi: [10.1093/mnras/stad1926](https://doi.org/10.1093/mnras/stad1926)

Schawinski, K., Koss, M., Berney, S., & Sartori, L. F. 2015, Monthly Notices of the Royal Astronomical Society, 451, 2517

Secunda, A., Bellovary, J., Mac Low, M.-M., et al. 2020, ApJ, 903, 133, doi: [10.3847/1538-4357/abbc1d](https://doi.org/10.3847/1538-4357/abbc1d)

Sirko, E., & Goodman, J. 2003, 341, 501, doi: [10.1046/j.1365-8711.2003.06431.x](https://doi.org/10.1046/j.1365-8711.2003.06431.x)

Soni, S., Berger, B. K., Davis, D., & et al. 2025, Classical and Quantum Gravity, 42, 085016, doi: [10.1088/1361-6382/adc4b6](https://doi.org/10.1088/1361-6382/adc4b6)

Stone, N. C., Metzger, B. D., & Haiman, Z. 2017, MNRAS, 464, 946, doi: [10.1093/mnras/stw2260](https://doi.org/10.1093/mnras/stw2260)

Tagawa, H., Haiman, Z., Bartos, I., & Kocsis, B. 2020, 899, 26, doi: [10.3847/1538-4357/aba2cc](https://doi.org/10.3847/1538-4357/aba2cc)

Tagawa, H., Kimura, S. S., Haiman, Z., Perna, R., & Bartos, I. 2023a, 950, 13, doi: [10.3847/1538-4357/acc4bb](https://doi.org/10.3847/1538-4357/acc4bb)

Tagawa, H., Kimura, S. S., Haiman, Z., Perna, R., & Bartos, I. 2023b, Shock cooling and breakout emission for optical flares associated with gravitational wave events, arXiv, doi: [10.48550/arXiv.2310.18392](https://doi.org/10.48550/arXiv.2310.18392)

Tagawa, H., Kimura, S. S., Haiman, Z., Perna, R., & Bartos, I. 2024, 966, 21, doi: [10.3847/1538-4357/ad2e0b](https://doi.org/10.3847/1538-4357/ad2e0b)

Tchekhovskoy, A., Narayan, R., & McKinney, J. C. 2011, MNRAS, 418, L79, doi: [10.1111/j.1745-3933.2011.01147.x](https://doi.org/10.1111/j.1745-3933.2011.01147.x)

The LIGO Scientific Collaboration, The Virgo Collaboration, & The KAGRA Collaboration. 2025a, GWTC-4.0: Updating the Gravitational-Wave Transient Catalog with Observations from the First Part of the Fourth LIGO-Virgo-KAGRA Observing Run, <https://arxiv.org/abs/2508.18082>

The LIGO Scientific Collaboration, The Virgo Collaboration, & the KAGRA Collaboration. 2025b, GW231123: a Binary Black Hole Merger with Total Mass  $190-265 M_{\odot}$ , <https://arxiv.org/abs/2507.08219>

Tomar, Y., Hopkins, P. F., & Kremer, K. 2026, arXiv e-prints, arXiv:2601.02487, doi: [10.48550/arXiv.2601.02487](https://doi.org/10.48550/arXiv.2601.02487)

Ulrich, M.-H., Maraschi, L., & Urry, C. M. 1997, ARA&A, 35, 445, doi: [10.1146/annurev.astro.35.1.445](https://doi.org/10.1146/annurev.astro.35.1.445)

Vaccaro, M. P., Mapelli, M., Périgois, C., et al. 2024, A&A, 685, A51, doi: [10.1051/0004-6361/202348509](https://doi.org/10.1051/0004-6361/202348509)

Vajpeyi, A., Thrane, E., Smith, R., McKernan, B., & Ford, K. E. S. 2022, 931, 82, doi: [10.3847/1538-4357/ac6180](https://doi.org/10.3847/1538-4357/ac6180)

Veronesi, N., van Velzen, S., & Rossi, E. M. 2025, MNRAS, 536, 3112, doi: [10.1093/mnras/stae2787](https://doi.org/10.1093/mnras/stae2787)

Wang, Y.-H., Lazzati, D., & Perna, R. 2022, MNRAS, 516, 5935, doi: [10.1093/mnras/stac1968](https://doi.org/10.1093/mnras/stac1968)

Ye, C. S., & Fishbach, M. 2024, ApJ, 967, 62, doi: [10.3847/1538-4357/ad3ba8](https://doi.org/10.3847/1538-4357/ad3ba8)

Zhang, H.-H., Zhu, J.-P., & Yu, Y.-W. 2024, 976, 63, doi: [10.3847/1538-4357/ad8139](https://doi.org/10.3847/1538-4357/ad8139)

Zhang, S.-R., Wang, Y., Yuan, Y.-F., et al. 2025, S241125n: Binary Black Hole Merger Produces Short GRB in AGN Disk, arXiv, doi: [10.48550/arXiv.2505.10395](https://doi.org/10.48550/arXiv.2505.10395)

Zhu, J.-P., Zhang, B., Yu, Y.-W., & Gao, H. 2021, ApJL, 906, L11, doi: [10.3847/2041-8213/abd412](https://doi.org/10.3847/2041-8213/abd412)

Zhu, L.-G., & Chen, X. 2025, Evidence of a fraction of LIGO/Virgo/KAGRA events coming from active galactic nuclei, arXiv, doi: [10.48550/arXiv.2505.02924](https://doi.org/10.48550/arXiv.2505.02924)

Zlochower, Y., Campanelli, M., & Lousto, C. O. 2011, Classical and Quantum Gravity, 28, 114015, doi: [10.1088/0264-9381/28/11/114015](https://doi.org/10.1088/0264-9381/28/11/114015)